6-9-2016

Catalyst Layer Design in Polymer Membrane Fuel Cells

Sarah Stariha

Sarah Stariha
Candidate

Chemical and Biological Engineering
Department

This dissertation is approved, and it is acceptable in quality and form for publication:

Approved by the Dissertation Committee:

Dr. Plamen Atanassov, Chairperson

Dr. Barr Halevi

Dr. Fernado Garzon

Dr. Kateryna Artyushkova

Dr. Alexey Serov

Dr. Andrew Schuler

CATALYST LAYER DESIGN IN POLYMER MEMBRANE FUEL CELLS

by

SARAH STARIHA

B.S., Chemistry, Beloit College, 2012

DISSERTATION

Submitted in Partial Fulfillment of the
Requirements for the Degree of

Doctor of Philosophy

Engineering

The University of New Mexico
Albuquerque, New Mexico

May, 2016

ACKNOWLEDGMENTS

I would like to thank my advisors Dr. Plamen Atanassov and Dr. Barr Halevi for their continued support and guidance. I would also like to thank my committee members Dr. Alexey Serov, Dr. Kateryna Artyushkova, Dr. Fernando Garzon, and Dr. Andrew Schuler. A special thanks to Dr. Alexey Serov, Dr. Kateryna Artyushkova, and Dr. Barr Halevi for their assistance in designing and executing these experiments. I would also like to acknowledge Pajarito Powder, LLC for letting me use their facilities over the past few years. This work would not have happened without them. I would like to thank Ted Thompson and Rita Remus-Thompson for the long hours of editing they have put into everything I have written. Together you two make the perfect duo. And last but certainly not least to my parents and sisters who have supported me in every crazy adventure I have undertaken. Without you guys I would not be the person I am today. This work was supported by DOE-EERE Fuel Cell Technology Program: "Development of Novel Non Pt Group Metal Electrocatalysts for PEMFC" (S.Mukerjee, PI) and DOE Incubator "Hydrogen Oxidation Reaction in Alkaline Media" (A. Serov, PI)

CATALYST LAYER DESIGN IN POLYMER MEMBRANE FUEL CELLS

by

SARAH STARIHA

B.S., Chemistry, Beloit College, 2012
Ph.D., Engineering, University of New Mexico, 2016

ABSTRACT

One of the biggest obstacles to commercializing polymer electrolyte membrane fuel cells is the use of platinum as a catalyst. One way to overcome this obstacle is to replace platinum with non-platinum group metal (non-PGM) catalysts, particularly for the oxygen reduction reaction (ORR) in proton exchange membrane fuel cells (PEMFCs). The most realistic method of estimating the performance of non-PGM catalysts is testing within membrane electrode assemblies (MEAs). One key issue is that non-PGM catalysts are not as active as platinum. One way to increase their performance is to optimize the catalyst layer composition, specifically the components responsible for ionic and electronic conductivity. The first objective of this work was to determine the optimal ionomer-to-catalyst ratio and additional carbon content within the catalyst layer. Another problem that arises when replacing platinum with non-PGM catalysts is the catalyst layer thickness. Platinum catalyst layers are on the order of 10 μm whereas non-PGM catalyst layers are on the order of 60-120 μm. Although this increase in catalyst allows for more active sites it causes challenges in transport performance by elongating pore channels. From this the second objective of this work was to examine the chemistry and morphology of both the non-PGM catalysts and sprayed catalyst layers and their effects on MEA performance.

Another polymer electrolyte membrane fuel cell and an alternative to PEMFCs are anion exchange membrane fuel cells (AEMFCs). Unlike the corrosive environment in PEMFCs, the alkaline environment of AEMFCs is much more conducive to non-PGM catalysts. The problem is that AEMFC technology is decades behind that of PEMFC, particularly the anion exchange membranes and their stability. Because of this there is very little data on alkaline MEA assembly and testing. The third objective of this work was to integrate new Ni-based hydrogen oxidation reaction (HOR) catalysts into alkaline MEAs. A large part of this objective was designing a reproducible protocol for making these MEAs.

From this work it was concluded that within the catalyst layer the amount of ionomer plays a key role in MEA performance as does any additional carbon added. In general higher amounts of Nafion® ionomer lead to poor overall performance most likely do to pore and active site blocking and loss of electronic conductivity. This can be corrected with the addition of carbon. It was found that the catalyst layer morphology also plays an important role in MEA performance, specifically pore connectivity. Lastly it was shown that a reproducible protocol for making alkaline MEAs was established and is comparable to what has been reported in the literature. Also initial MEA data for Nickel-Molybdenum-Copper HOR catalysts was successfully acquired for the first time.

TABLE OF CONTENTS

LIST OF ABBREVATIONS

PEMFC – Proton Exchange Membrane Fuel Cell
AEMFC – Alkaline Exchange Membrane Fuel Cell
MEA– Membrane Electrode Assembly
HOR– Hydrogen Oxidation Reaction
ORR– Oxygen Reduction Reaction
AFC– Alkaline Fuel Cell
Non-PGM– non-Platinum Group Metal
M-N-C– Metal Nitrogen Carbon
SSM– Sacrificial Support Method
SEM– Scanning Electron Microscope
TEM– Transmission Electron Microscope
XPS– X-ray Photoelectron Spectroscopy
DFT– Density Functional Theory
Ni– Nickel
O– Oxygen
Ni-Mo-M– Nickel-Molybdenum-Metal
DOE– Department of Energy
GDL– Gas Diffusion Layer
CCS– Catalyst Coated Substrate
GDE– Gas Diffusion Electrode
PTFE– Polytetrafluoroethylene
AEM– Alkaline Exchange Membrane
Vulcan– Vulcan XC72R
KB600– Ketjen Black 600 EC
CNTs– Carbon Nanotubes
KE– Kinetic Energy
BE– Binding Energy
PCA– Principle Component Analysis
NCB– Nicarbazin
SGB– Sulfaguanidine
MBZ– Mebendazole
BET– Brunauer-Emmett-Teller
FEG– Field Emission Gun
FIB– Focused Ion Beam
Ni-Mo-Cu– Nickel-Molybdenum-Copper
CCM– Catalyst Coated Membrane
UR– Urea
MM– Melamine
Fe- Iron

1. INTRODUCTION

Clean energy sources are currently in high demand. Fuel cells, with their zero emissions, are a potential solution. They offer a wide range of applications from high temperature stationary power generation to low temperature portable power sources. For portable applications, such as vehicles, polymer electrolyte membrane fuel cells are very attractive due to their low operating temperature, quick start up, high efficiency, and high power density.(*1*) There are two main types of polymer electrolyte membrane fuel cells currently being developed, proton exchange membrane fuel cells (PEMFCs) and alkaline exchange membrane fuel cells (AEMFCs).

PEMFCs were invented in 1955 by William Grubb at General Electric but it's only been in the past three decades that PEMFC research and development has significantly expanded.(*2*) PEMFCs consist of three main parts: an anode, a cathode, and a membrane electrode assembly (MEA). See Figure 1. H_2 enters on the anode side where it is split into protons and electrons. See Equation 1. The protons are transported through the solid ionomer membrane while the electrons are transported through an external circuit to produce electricity. O_2 enters the cathode side where it is split into single oxygen molecules during the oxygen reduction reaction (ORR). Two single oxygen molecules react with four protons and four electrons to make two molecules of water. See Equation 2.

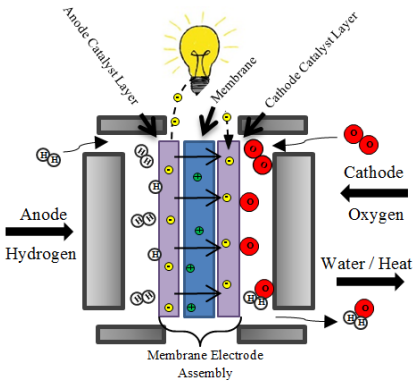

Figure 1. Diagram of Proton Exchange Membrane Fuel Cell (PEMFC).

Anode:	$2H_2 \rightarrow 4e^- + 4H^+$	E = 0.00 V	**Eq. 1**(*3*)
Cathode:	$O_2 + 4e^- + 4H^+ \rightarrow 2H_2O$	E = 1.23 V	**Eq. 2**(*3*)
Overall:	$2H_2 + O_2 \rightarrow 2H_2O$	E = 1.23 V	**Eq. 3**

The alkaline fuel cell (AFC) was invented by Francis Thomas Bacon in 1933. It consisted of a liquid alkaline electrolyte, a concept that would continue into the 1960s when AFCs with liquid KOH electrolytes were used for the U.S. Apollo space missions.(*2*) However liquid electrolytes were easily poisoned from CO_2 in air. The CO_2 would react with the mobile cations (K^+) to form solid crystals of metal carbonates that would block any reaction from taking place.(*4*) For this reason AFC research was dropped in the late 1970s and PEMFCs took over as the polymer membrane fuel cell of choice due to its solid membrane electrolyte. McLean *et al.* wrote in 2002 in response to what could improve AFCs "The solid ionomer alkaline membrane is intriguing because it suggests one possible path for developing AFC systems combining the desirable properties of a solid electrolyte with the fast anode reaction kinetics of an alkaline cell. Unfortunately, no further developments achieved with this technology have been

published, leading us to conclude that the work has been discontinued."(5) This is a testament to the current stage of AEMFC research and technology.

AEMFCs operate similarly but not identically to PEMFCs. Like PEMFCs, AEMFCs consist of three main parts: an anode, a cathode, and a MEA. H_2 enters on the anode side where it is split into protons and electrons. See Equation 4. Electrons are transported through an external circuit to produce electricity, however unlike the PEMFC, the protons stay on the anode side. Both O_2 and water enter the cathode side where they are split in order to form OH^- anions during the ORR. The OH^- anions are transported from the cathode to the anode through the solid alkaline exchange membrane. Once at the anode four OH^- anions combine with two protons and an electron to form water during the hydrogen oxidation reaction (HOR). See Equation 5.

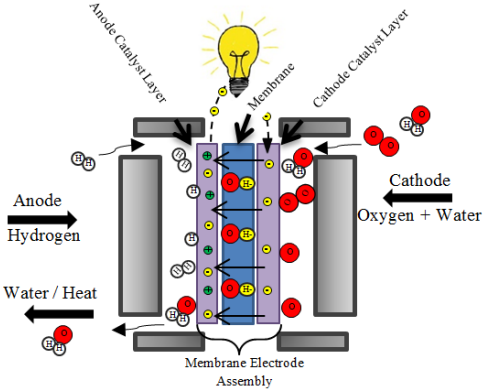

Figure 2. Diagram of Alkaline Exchange Membrane Fuel Cell (AEMFC).

Anode:	$2H_2 + 4OH^- \rightarrow 4H_2O + 4e^-$	E = -0.828 V	**Eq. 4**(*3*)
Cathode:	$O_2 + 2H_2O + 4e^- \rightarrow 4\ OH^-$	E = 0.401 V	**Eq. 5**(*3*)
Overall:	$2H_2 + O_2 \rightarrow 2H_2O$	E = 1.23 V	**Eq. 6**

Even though the overall reaction is the same for both PEMFCs and AEMFCs, see Equations 3 and 6, there are two very important differences that should be noted: (a) Water is generated at the cathode for PEMFCS but at the anode from AEMFCs (b) Water is a direct reactant in AEMFCs as it is consumed in the cathode reaction.(*3*)

There are advantages and disadvantages for both PEMFCs and AEMFCs. For PEMFCs the advantages lay in it's the well developed technology: fast HOR kinetics and stable ionomer and membrane. The disadvantages however are that there is still a lack of a cost-effective, efficient catalyst for the slow ORR reaction, fuel is limited to pure H_2 due to poisoning, and a corrosive environment where only precious metals are durable.(*6*) The advantages of AEMFCs correspond to the disadvantages of PEMFCs and stem from the alkaline pH environment. They have fast ORR kinetics and they can use non-precious metal catalysts. They also have a wider choice of fuels. In addition to pure H_2, unclean H_2 can also be used along with hydrazine. However AEMFCs have slow HOR kinetics and low ionic conductivity and stability of both ionomers and membranes.(*3, 7*) Because of these advantages and disadvantages research and development for both PEMFCs and AEMFCs continue to be a rapidly growing field.

Non-Platinum Metal Group Catalysts

Current PEMFC technologies use platinum catalysts for both the anode and the cathode which are extremely expensive and account for over 40% of the total cell cost.(*8*) Because of this, there has been a huge push to develop non-platinum group metal (non-PGM) catalysts. This is slightly easier for the anode as the HOR kinetics are much faster than the ORR kinetics on the cathode.(*9, 10*) The ORR kinetics, even on platinum

catalysts, account for over 50% of the total cell voltage loss with an overpotential on the order of 300-400 mV compared to the HOR kinetics with an overpotential of less than 5 mV.(*11*)

One rapidly developing class of non-PGM catalysts for ORR is nanomaterials based on transition metal-nitrogen-carbon networks (M-N-C). These M-N-C non-PGM catalysts are made from transition metal salts and nitrogen-containing organic precursors. In order for non-PGM catalysts to achieve their highest catalytic activity, they must have a well-developed pore structure and high density of active sites. For more than a decade, the University of New Mexico has been developing an original synthesis method for non-PGM catalysts and other classes of materials, called the Sacrificial Support Method (SSM).(*12-16*) SSM produces materials with open-frame hierarchical morphology at the micro- and meso-scale. See Figure 3. SSM is based on the infusion of silica particles with transition metal and organic precursors. After high temperature pyrolysis in an inert atmosphere, the silica template is etched away leaving a self-supported M-N-C catalyst with tailored mesoporosity. By using templates with different sizes, surface area can be tuned, and pore size distribution can be tailored over a range of 10-500 nm.

(A) 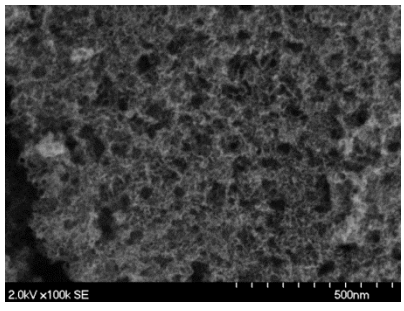

(B) 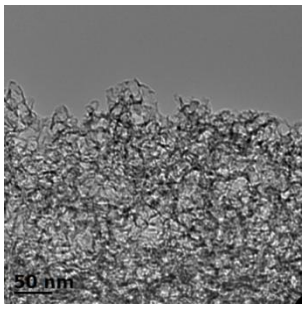

Figure 3. Images of a non-PGM M-N-C ORR catalyst for PEMFCs prepared by Sacrificial Support Method **(A)** SEM and **(B)** TEM.

It is widely acknowledged that nitrogen from the organic precursors plays an important role in the ORR mechanism, however the exact extent to which it contributes to the possible active sites is a topic of study in itself.(*17-20*) Through a combination of x-ray photoelectron spectroscopy (XPS) and density functional theory (DFT) calculations it has been suggested that nitrogen stabilizes the attachment of the transition metals to the underlying carbon support creating the ORR active sites.(*21-23*) A variety of transition metals have been studied with iron being the most commonly used.(*20, 24*) Different organic precursors have been examined and their results published. They include Co-tetramethoxy phenylporphyrin,(*25*) poly(ethyleneimine),(*26*) 4-aminoantipyrine,(*8*) and carbendazim.(*13*)

Unlike non-PGM catalysts in PEMFCs, there is considerably less research into non-PGM catalysts in AEMFCs. The alkaline environment is actually more conducive to non-PGM catalysts, especially for the ORR. It has been reported that typically the ORR on carbon supported platinum proceeds through a 4 electron path in acid, however in alkaline it proceeds through a two electron outer sphere charge transfer process producing a peroxide anion intermediate followed by an additional 2 electron reduction step to produce water. This is believed to occur because specifically adsorbed hydroxyl species interact with solvated oxygen molecules. The same report showed that in contrast to this a non-PGM catalyst exhibited an exclusive inner sphere 4 electron reduction in alkaline due to direct adsorption of oxygen and the kinetically favored hydrogen peroxide reduction reaction making it a better ORR catalyst in this case than platinum.(*27, 28*) Catalyst stability is also less of an issue in an alkaline environment. In acid low non-PGM

stability is due to the oxidative corrosion of the carbon support and active site poisoning by hydrogen peroxide that is formed during the two-electron reduction of oxygen.(*29, 30*)

In contrast, the challenge in AEMFCs is the anode catalyst. In alkaline the HOR kinetics are two orders of magnitude slower on platinum catalysts than in acid. This equates to an overpotential between 130-150 mV.(*3, 11*) It is believed that platinum's lack of HOR catalytic activity in alkaline is due to the metal's lack of tendency to form OH_{ads} species from the OH^-_{aq} anions at the negative potentials associated with good anode performance.(*31*)

One class of materials being considered to replace platinum as the HOR catalyst in alkaline media is nickel (Ni)-based nanoparticles. Ni is believed to be able to help bond OH^- surface species to hydrogen atom intermediates on the anode to aid in the formation of the produced water molecules.(*31*) The issue, however, is that such Ni catalysts have shown electrode potentials similar to nickel oxides. According to DFT calculations, H adsorbs almost only to the bottom of the sp-band on the Ni surface. O adsorbs predominately to the d-band which makes a strong bond between O_{ads} and the free electrons of the Ni surface. If Ni's d-band can be suppressed while retaining the sp-band then the Ni-O bond would be selectively weakened with little influence on the surface formation of Ni-H bonds. One possible way to achieve this d-band suppression is to combine the Ni with transition metal oxides.(*32*)

Nickel-Molybdenum-metal (Ni-Mo-M) materials have shown great promise as non-PGM HOR catalysts in alkaline.(*6*) In the past year the University of New Mexico has been developing unsupported Ni-Mo-M catalysts that show good HOR activity. These materials are synthesized using a solid state method that combines solid nitrites

and Mo-salt. This is ground, dried and finally reduced resulting in a catalyst with a relatively low surface area but well-developed morphology. See Figure 4.

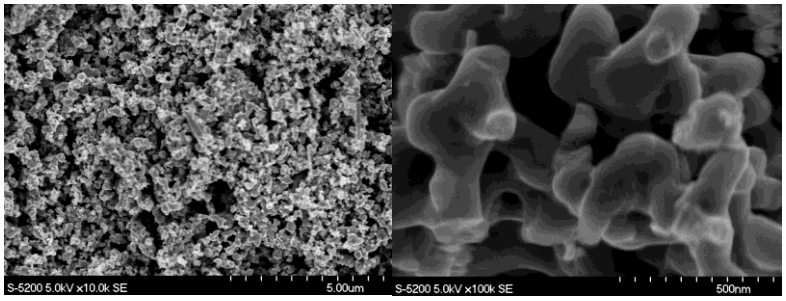

Figure 4. SEM images of a non-PGM Ni-Mo-M HOR catalyst for AEMFCs prepared by a solid state method.

The Role of Ionomer in the Membrane Electrode Assembly

The most realistic method of estimating catalytic performance of non-PGM catalysts is testing within MEA configurations. This type of testing can be done according to the US Department of Energy (DOE) recommended protocol.(*33*) The MEA is the central part of the fuel cell and consists of the anode and the cathode catalyst layers, both backed by a gas diffusion layer (GDL). The GDL acts as both mechanical support and as a media for the transport of gases and water in and out of the catalyst layer. The catalyst layer can be attached to the GDL, called a catalyst coated substrate (CCS) or more commonly a gas diffusion electrode (GDE). The catalyst layers are separated by an ionomer membrane. See Figure 5. In PEMFCs Nafion® is the most commonly used ionomer membrane. The catalyst layer can then be separated into the catalyst itself and the ionomer.

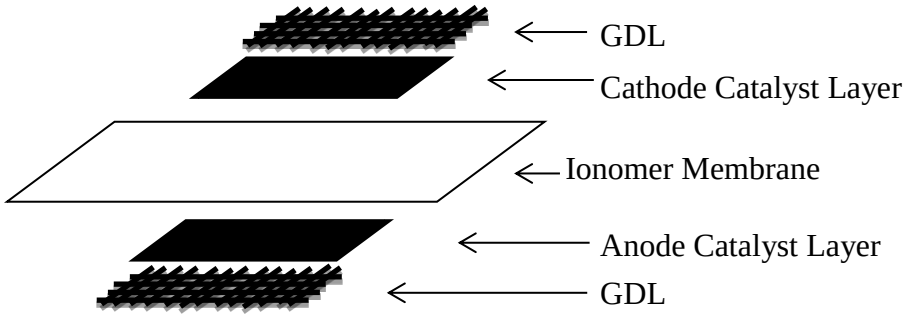

Figure. 5 Diagram of Membrane Electrode Assembly.

Within the catalyst layer there is a complex interplay between the catalyst and the ionomer affecting the cell's overall performance.(*34-36*) In PEMFCs the Nafion® ionomer is responsible for transporting protons, also called ions, to the active sites and serves as a media to remove water from the active sites.

The Nafion® ionomer consists of perfluorosulfonic acid (PFSA) chains comprised of a polytetrafluoroethylene (PTFE) backbone with attached sulfonate heads (SO_3^-). See Figure 6.(*37*) The PTFE backbone is extremely hydrophobic, meaning it repels water, which aids in product water transport, both liquid and vapor, from the active sites. The negative charge on the sulfonate heads allows the position protons to "hop" from head to head and move across the Nafion® membrane along Nafion® ionomer channels into the active sites. In reality, the protons are strongly associated with water molecules and are transported in the form of H_3O^+ hydronium ions, or even higher order cations.(*37*) Water plays a vital role in the cell's overall performance. In order for the Nafion® ionomer membrane to maintain high proton conductivity a sufficient amount of water is required, however, excess liquid water in the cell can flood and block the pores of the catalyst layer and GDL. On the other hand if there is too little liquid water then the

Nafion® ionomer membrane and channels dry out and proton conductivity is lost. Both drying and flooding lead to loss of the cell's performance. (*38, 39*)

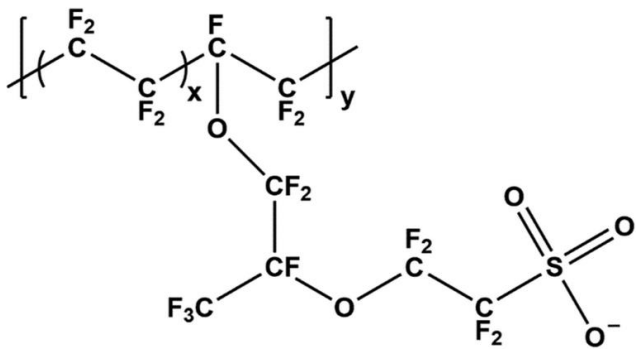

Figure 6. Structure of perfluorosulfonic acid (PFSA) chain.

The effect of ionomer to catalyst ratio on the performance has to be understood and optimized. For any particular catalyst, there is an optimal amount of ionomer within the catalyst layer that results in the best performance. While the kinetic performance improves with higher ionomer content, likely due to better ionic transport and conductivity, the mass transport is hindered due to excess ionomer or water blocking the pores. Previous work has been done to examine the effect of catalyst to ionomer ratio in platinum based catalysts. These studies show that systems with lower catalyst to ionomer ratios between 10-30wt% have the best performance.(*40-43*) More recently there have been a number of publications presenting MEA performance data using non-PGM ORR catalysts.(*44*) These studies looked at weight percentages of Nafion® ranging from 25wt% to 75wt%. In both studies, the best performing MEAs were those made with 50wt% Nafion® while higher Nafion® containing inks performed significantly worse.(*25, 45*) There is a tendency for a decrease in the overall performance when higher amounts

of Nafion® are used.(*46*) One of the possible explanations for this loss in performance is that the excess Nafion® is separating the catalyst particles, breaking the electronic pathway and losing electronic conductivity.

One way of compensating this process is to add conductive material, such as carbon, to the catalyst before integration into the MEA. Carbon additives can act as a bridge, interconnecting catalyst particles and re-establishing a continuous electronic pathway. Ideal carbon additives should improve conductivity but should not change the composition of the M-N-C catalysts by introducing chemical groups that may compromise its hydrophobic properties and stability. Introduction of amorphous carbon with surface oxides may increase hydrophilicity of the catalysts, results in flooding and increase carbon corrosion compromising activity and stability of the catalysts.(*44*)

Unlike PEM membranes such as Nafion®, alkaline membrane technology is a few decades behind and one of the major factors that is prohibiting AEMFC commercialization.(*3, 47, 48*) There are many challenges facing alkaline exchange membranes (AEMs). One of them is ionic conductivity. According to Table 1, OH^- has a lower mobility than H+ most likely due to the relative size of the OH^- ion compared to that of the H^+ ion. The polymer framework of the AEM may also be slowing down OH^- mobility (*3*)

Ion	Mobility (μ)/10^{-8} $m^2s^{-1}v^{-1}$	Relative mobility (relative to K^+)
H^+	36.23	4.75
OH^-	20.64	2.71
CO_3^{2-}	7.46	0.98
HCO^{3-}	4.61	0.60
Na^+	5.19	0.68
Cl^-	7.91	1.04
K^+	7.62	1.00

Table 1. Select ion mobilities (μ) at infinite dilution in H2O at 298.15 K(*3*).

Like the conduction of H^+ ions, the conduction of OH^- also relies on water within the membrane and the presence of a hydrophilic domain. It is believed that the high ionic conductivity of Nafion® is due to the morphological phase segregation of the hydrophobic backbone and the hydrophilic side chains that when overlapped form interconnected channels that increase the H^+ "hopping" efficiency.(*3*) The phase segregation in AEMs is not as well defined since most are based on hydrocarbon backbones with lower hydrophobicites compared to Nafion®'s PTFE backbone. AEM side chains are frequently connected by short hydro-carbon links that also lower the hydrophobicity. Hydrophobicity is further compromised by the cationic head groups used, such as quaternary compounds like quaternary ammonium.(*49*) See Figure 7.

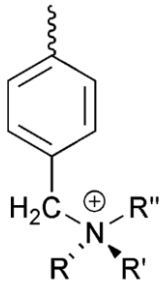

Figure 7. Structure of Quaternary Ammonium.

Stability is the other key challenge in AEMs. Although they need to be in the OH^- form when operating in the fuel cell, when outside the cell membranes in OH^- form are very unstable. First, in the presence of air OH^- membranes convert to less conductive CO_3^{2-} or even less HCO_3^-. Second the cationic groups can't always survive and may decompose in the presence of OH^-.(*3, 4, 47*) The main method that has been employed to help combat these issues is to make the membrane in a bromide or chloride form which is very stable dry when outside the cell. The membrane is then exchanged into the OH^- form

before testing by soaking it in either NaOH or KOH and rinsed with deionized water. (*3*, *47*, *50*)

Evaluating Membrane Electrode Assembly Performance

One of the easiest and quickest methods to testing MEA performance is through polarization curves. One common method for acquiring polarization curves is potentiostatically, meaning the potential is held constant while the resulting current is measured and plotted over a set potential range, usually from 1.0 V to 0.3 V. See Figure 8.

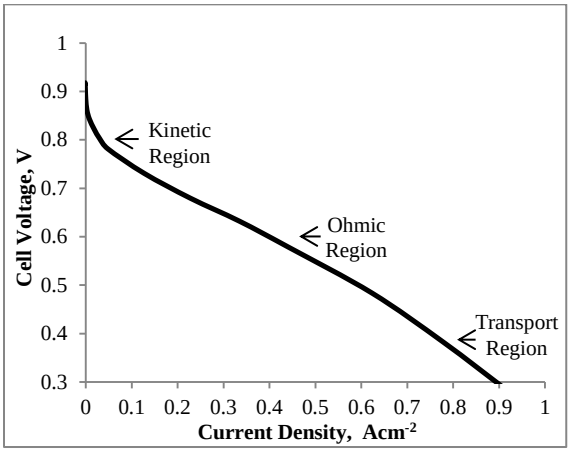

Figure 8. Polarization Curve.

There are three regions of a polarization curve that contribute to the measured cell voltage: kinetic, ohmic, and transport. The kinetic region near 0.8 V indicates the catalytic reaction efficiency. The ohmic region around 0.6 V indicates the ionic and electronic resistances in the cell. These resistances encompass all components including ionic resistance in the membrane, ionic and electronic resistance in the electrodes, and

electronic resistance in the GDL and cell hardware. Lastly, the transport region near 0.4 V indicates the efficiency of moving reactant gases and water to and from the active sites.

Each region of the polarization curve is governed by its own set of equations that include equations for the conservation of mass, momentum, energy and charge transport with expressions for overall kinetics and thermodynamics. The catalyst layer is the most complex layer within the MEA and its governing equations must account for the microscopic heterogeneity of its porous structure and the multiphase flow that is occurring. It should be noted that the equations below are based on platinum catalyst layers and assume agglomerate catalyst particles with a defined diameter and spherical pores with a defined radius. (*51*)

The kinetic region is governed by a modified Tafel approximation with a dependence on oxygen partial pressure (P_{O_2}) and an Arrhenius temperature dependence ($\frac{-\alpha_c F}{RT}(\eta_{ORR})$) for the exchange current density ($i_{0_{ORR}}$). Here $\alpha_c, F, R, T,$ and η_{ORR} represent the cathode charge transfer coefficient, Faraday's constant, ideal-gas constant, and absolute temperature, respectively. The four-electron ORR involves the formation of oxides which can block active sites and needs to be taken into account. Oxide formation involves oxide coverage (Θ_{oxide}) and the energy for oxide adsorption (ϖ). The resulting ORR current density (i_{ORR}) governing equation is also dependent on the acid or base concentration (a_{HM}) in the ionomer.(*51*) See Equation 7.

$$i_{ORR} = -i_{0_{ORR}}(1-\Theta_{oxide})\left(\frac{P_{O_2}}{P_{O_2}^{ref}}\right)^{m_0}\left(\frac{a_{HM}}{a_{HM}^{ref}}\right)^2 exp\left(\frac{-\alpha_c F}{RT}(\eta_{ORR})\right) exp\left(\frac{-\varpi\Theta_{oxide}}{RT}\right) \quad \textbf{Eq. 7}$$

For the ohmic region it is important that the governing equation have expressions that represent the transfer current between the electronic and ionic conducting phases as a function of local conditions in the catalyst layer. This is a challenge because there is little knowledge of the structure/function relationship of the ionomer in the catalyst layer therefore the concentrated-solution theory used for bulk membrane can be applied.(*51*) See Equations 8 and 9.

$$i_{ionomer} = -\kappa \nabla \Phi_{ionomer} - \frac{\kappa \xi}{F} \nabla \mu_w \qquad \textbf{Eq. 8}$$

$$N_w = -\frac{\kappa \xi}{F} \nabla \Phi_{ionomer} - \left(\alpha + \frac{\kappa \xi^2}{F^2}\right) \nabla \mu_w \qquad \textbf{Eq. 9}$$

Here κ is the ionic conductivity, Φ_{proton} is the electrostatic potential of the ionomer, and ξ is the electro-osmotic coefficient. ξ is defined as the ratio of the flux of water to the flux of protons in the absence of a concentration gradient. N_w is the superficial flux of water, α is the transport parameter that can be related to hydraulic pressure or the concentration gradient though the chemical-potential driving force ($\nabla \mu_w$).(*51*) See Equation 10.

$$\nabla \mu_w = RT \nabla ln a_w + \bar{V}_w \nabla p \qquad \textbf{Eq. 10}$$

Here a_w, $\bar{V}_w$, and p are the activity, molar volume and hydraulic pressure of water.

Next the transfer current between the electronic-conducting (1) and ionic-conducting (2) phases need to be taken into account.(*51*) See Equation 11.

$$\nabla \cdot i_2 = -\nabla \cdot i_1 = a_{1,2} i_{h,1-2} \quad \textbf{Eq. 11}$$

Here the interfacial area of the catalyst with respect to the ionomer and gaseous reactants ($a_{1,2}$) is equal to the catalyst loading ($m_{catalyst}$) and surface area ($A_{catalyst}$) divided by the catalyst layer thickness (L). However if there is liquid water present in the catalyst layer it will block some of the active sites. This is represented by adding specific interfacial area with no blockage ($a_{1,2}^{\circ}$) and saturation (S) .(*51*) See Equation 12.

$$a_{1,2} = \frac{m_{catalyst} A_{catalyst}}{L} = a_{1,2}^{\circ}(1 - S) \quad \textbf{Eq. 12}$$

The transport region is largely dependent on the catalyst layer structure. This can be shown by modifying the transfer-current source term to account for diffusional losses on the agglomerate scale.(*51*) See Equation 13.

$$\nabla \cdot i_2 = a_{1,2} i_{h,1-2} \mathrm{E} \quad \textbf{Eq. 13}$$

Here E is an effectiveness factor which is defined as the actual reaction rate to the rate if all the agglomerate was available for reaction.(*51*) See Equation 14.

$$E = \frac{4\pi R_{agg}^3 \left(-D_{O_2}^{eff} \frac{dc_{O_2}}{dr} \Big]_{r=r_{agg}} \right)}{\frac{4}{3}\pi R_{agg}^3 \left(-k_{s,m_0} c_{O_2,s}^{m_0} \right)} \quad \textbf{Eq. 14}$$

Here R_{agg} is the agglomerate radius, k_{s,m_0} is the ORR rate at the surface, $c_{O_2,s}^{m_0}$ is the concentration of oxygen at the surface and $D_{O_2}^{eff}$ is the effective oxygen diffusion and can be solved using Equation 15 where *d* is the pore diameter.(*51*)

$$D = \frac{d}{3}\left(\frac{8RT}{\pi M_i}\right)^{\frac{1}{2}} \qquad \textbf{Eq. 15}$$

Although polarization curves cannot separate out individual microscopic phenomena occurring within the catalyst layer they give enough information to be able to compare multiple MEAs at a time and determine, in general, the limiting region.

2. STATEMENT OF RESEARCH PROBLEMS AND OBJECTIVES

The limiting reaction in a PEMFC is the ORR as it is seven times slower than the HOR and presents a significant challenge to increasing PEMFC performance.(*9, 10*) Due to platinum's price, when it is used as the ORR catalyst the smallest amount possible is utilized. The current DOE target is a total of 0.125 $mg_{Pt}\,cm^{-2}$ for both the anode and the cathode. This very low platinum loading leads to very thin catalyst layers (~10 μm).(*52*) Non-PGM catalysts for ORR are not as active as platinum catalysts however because they are significantly cheaper more catalyst can be used per electrode. Approximately 4 mg cm^{-2} loading of non-PGM catalyst is used per cathode which makes the catalyst layer very thick (60-120 μm).(*53*) Although this increase in catalyst amount allows for more active sites and higher kinetic performance it causes challenges in the coupled transport of oxygen, water, protons, and electrons that takes place within the catalyst layer.(*54*)

Another major difference between platinum and non-PGM catalyst layers is the structure of the catalyst itself. See Figure 9. Platinum catalysts are primary made of a carbon support with intermittent platinum particles making a layer consisting of many agglomerates clustered together. Non-PGM catalysts on the other hand have a very open structure.

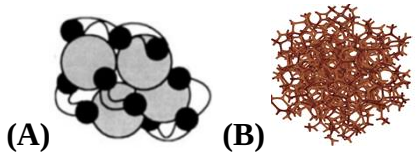

Figure 9. (A) Structure of Platinum Catalyst Supported on Carbon(*1*) **(B)** Open Structure of Non-PGM Catalyst.

The difference in catalyst structure and the difference in catalyst layer thickness are the two biggest challenges that are present when optimizing non-PGM catalyst layers. The goal of this work is twofold; the first part is to optimization the Nafion® ionomer and additional carbon content within the catalyst layer. As mentioned above the Nafion® ionomer's role is ionic conductivity. The second part is to examine the morphology and chemistry of the catalyst and sprayed catalyst layers and their effect on MEA performance.

As previously mentioned, one of the biggest hurdles to overcome with AEMFCs is the lack of stable and durable membranes. Because of this there is very little data on alkaline MEA assembly and testing. From the available literature only two groups reported successfully making and testing completely platinum-free alkaline MEAs.(*31, 32, 55*) Other groups have focused on optimizing commercial alkaline membranes using platinum as one or both electrodes. (*30, 56, 57*) The main goal of this project was to

integrate new Ni-based HOR catalysts into an alkaline MEA. Since there is so little literature on making alkaline MEAs, this project included designing a reproducible MEA assembly protocol.

The **first objective was to determine the optimal Nafion® ionomer-to-catalyst ratio and additional carbon content with respect to MEA performance.** Part of the cathode catalyst layer's role in PEMFCs is the conductivity of ions and electrons needed for ORR. The Nafion® ionomer is responsible for the ionic conductivity while carbon from the precursors is responsible for the electronic conductivity. The relationship between these conductivities and the overall performance is expressed in Equations 16 and 17 where κ_i and κ_e are ionic and electronic conductivity, and V_i and V_e are ionic and electronic potential.(*53*)

$$0 = -\kappa_i \nabla^2 V_i - nFr_{ORR} \quad \textbf{Eq. 16}$$

$$0 = -\kappa_e \nabla^2 V_e + nFr_{ORR} \quad \textbf{Eq. 17}$$

Enhancing these conductivities comes from optimizing the catalyst layer composition. For this objective three different Nafion® ionomer ratios were examined with the working theory that an increase in Nafion® ionomer will increase the ionic conductivity which will increase the overall performance. However as also mentioned too much ionomer will potentially decrease the electronic conductivity within the catalyst layer. To counter this three different types of carbon; Vulcan XC72R (Vulcan), Ketjen Black 600 (KB600), and in-house synthesized carbon nanotubes (CNTs) were introduced into the catalyst layer

with the theory that they will increase electronic conductivity which will lead to an increase in overall performance.

The second objective was to examine the chemistry and morphology of both the non-PGM catalyst and sprayed catalyst layer and their effects on MEA performance. The other role of the cathode catalyst layer in PEMFCs is the transport of oxygen and water used and produced during the ORR. This is made more difficult by the increased catalyst layer thickness of non-PGM catalysts. Transport losses can be identified using MEA testing however it is important to pinpoint what about the catalyst layer could be causing these losses. For this objective three different catalysts and their sprayed layers were compared using their chemistry and morphology.

The **third objective was to integrate non-PGM HOR catalysts into Alkaline MEAs.** The role of the HOR catalyst layer in AEMFCs is very important as it is the location of the limiting reaction within the cell. Although the alkaline environment is more conducive to non-PGM catalysts, nickel's affinity to oxidize at positive potentials poses a huge challenge. See Figure 10. This pourbaix diagram depicts the potentials were nickel is most stable in alkaline.(*58*)

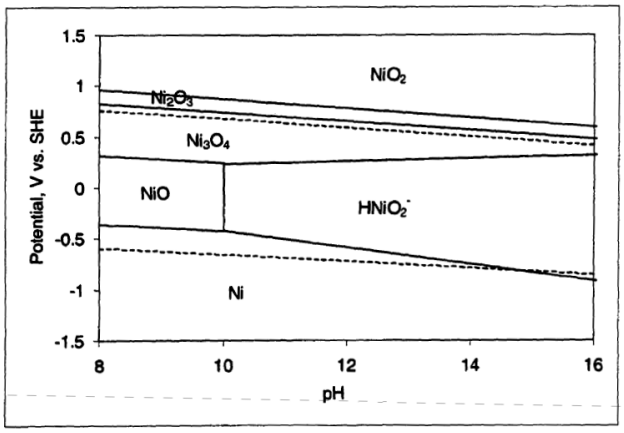

Figure 10. Pourbaix diagram of nickel in water at 70 °C.

Part of this objective was to integrate Ni-based catalysts into MEAs, which proved to be quite challenging. Because AEMFC technology is still developing, particularly alkaline membranes, very few groups have reported successfully obtaining alkaline MEA data. The other part of this objective was to develop a protocol for making and alkaline MEAs.

3. RESEARCH DESIGN

3.1 OBJECTIVE 1: Optimization of Nafion® Ionomer-to-Catalyst Ratio and Additional Carbon Content

The first objective was to determine an optimized amount of Nafion® ionomer and additional carbon content within the catalyst layer. For this study in order to increase the amount of nitrogen surface species two different nitrogen-rich organic precursors were used, urea (UR) and melamine (MM). See Figure 11. The catalysts studied were synthesized by modified SSM.(*13*) Iron nitrate (2.5 g, $Fe(NO_3)_3*9H_2O$, Sigma Aldrich) was mechanically mixed with 25 g of nicarbazin (NCB, Sigma Aldrich) and 10 g of LM150 fumed silica (Cabot, surface area ~150 $m^2\ g^{-1}$). Pre-mixed material was loaded into a 100 mL agate ball-mill jar with 16 agate balls (diameter 1 cm). Mixture was subjected to ball-milling at 450 rpm for 1 hour using an Across International PQ-N04 Planetary ball mill. Homogenous powder was pyrolyzed at 950 °C for 30 min in the flow of Ultra High Purity (UHP) nitrogen, 100 ccm. After heat treatment, silica was removed by 25wt% HF, followed by washing with deionized (DI) water until neutral pH was reached. Obtained powder was dried overnight at 85 °C. In order to remove un-washed H_2SiF_6, second treatment in a reactive atmosphere (10% NH_3, 100 ccm) was performed at

975 °C for 30 min. The additional ball-milling with nitrogen-rich organic precursors; UR and MM (in the ratio of 1 g of non-PGM catalyst to 2.5 g of UR or MM) followed by heat treatment in UHP nitrogen at 950 °C for 30 min was performed in order to increase density of active sites.

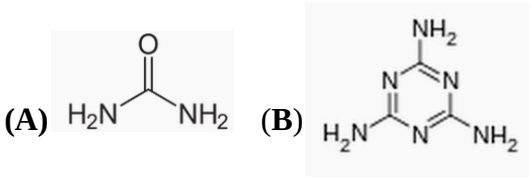

Figure 11. Chemical structures of **(A)** Urea **(B)** Melamine.

A standard cathode ink was prepared as follows: 180 mg non-PGM catalyst and 7.9 mg 2:1 isopropanol/deionized water (IPA/DI H_2O) solution, while the amount of the Nafion® ionomer was adjusted to be 45wt%. The mixture was homogenized by a high energy homogenizer (IKA) at 18000 rpm for 90 min using a 10 mm diameter rod. The ink was sprayed on carbon paper (SGL, 25BC) using an air brush. Catalyst loading was 4.0 mg cm^{-2} ± 0.5. An additional Nafion® layer was then sprayed with a 0.3 mg cm^{-2} loading in order to prevent GDE delamination.

The standard ink formulation was varied to make inks with 25wt% and 35wt% Nafion® and inks with carbon additives. For inks with carbon additives, 144 mg non-PGM catalyst and 36 mg carbon (20wt% Vulcan, KB600 and CNTs) were used. The purpose of adding additional carbon to the ink was to increase electronic conductivity. Vulcan was selected because it is an industry standard carbon black. KB600 was selected because it is hydrophobic. CNTs were selected because they were acid treated making them hydrophilic. Before being integrated into the MEA bulk electronic conductivity

measurements were taken for the powder catalysts both with and without carbon to see if electronic conductivity was actually being increased with the additional carbon.

In order to test the catalyst the GDE was assembled into an MEA. The MEA was assembled using a 125 μm thick gasket on the anode and 250 μm thick gasket on the cathode. The anode (0.4 mg_{Pt} cm^{-2}), membrane (Nafion® 211), and the cathode was pressed in a heated Carver press at 500 psi at 130 °C for 10 min. The MEA was placed in a 5 cm^2 cell with serpentine flow channels, and bolts were tightened to 40 inch-pounds. A Fuel Cell Technologies test station was used to obtain H_2/air polarization curves. The anode and cathode gases were heated and fully humidified at 85 °C, and the flow rates were 200 and 250 sccm, respectively. The cell operating temperature was maintained at 80 °C. Polarization curves were acquired potientiostaticly with a 60 sec delay before data acquisition at 12 $(0.8\ bar)_{gauge}$ and 30 $(2\ bar)_{gauge}$ psi backpressure.

In order to measure bulk electronic conductivity an in-house measurement system was set up. The powder was placed in a Teflon casing with gold electrodes on either end. See Figure 12. The bulk electronic conductivity was measured under 167 and 1111 psi of pressure. The presented pressing conditions were selected in order to assure that there was good electronic contact between the powder and the electrodes. On the other hand, taking into account the open-framed structure of the catalyst one should be extremely careful in order not to over-press the catalyst, but instead get a sense of the bulk electronic conductivity of the powder as a measure of how it packs. The pressing was done in air at room temperature.

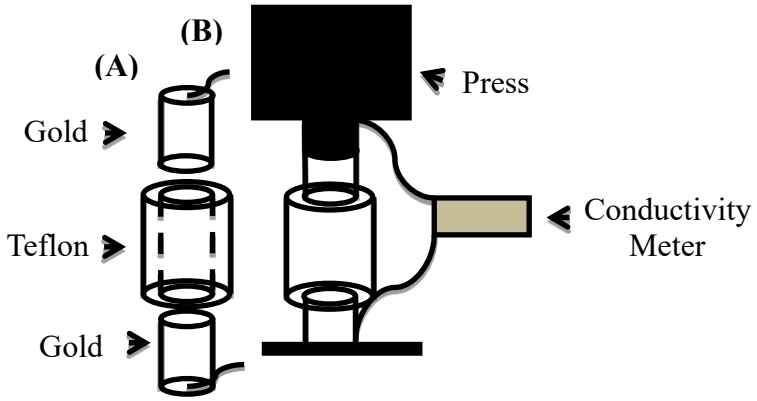

Figure 12. Set-up of in-house bulk conductivity measurement system. **(A)** Teflon casing with the two gold electrodes **(B)** Teflon casing with gold electrodes in press connected to conductivity meter.

To determine the effect of the additional carbon on the chemical composition of the catalyst all the powers were analyzed using XPS. The XPS spectra were acquired using a Kratos AXIS DLD Ultra photoelectron spectrometer using a monochromatic Al Kα source. Data analysis and quantification was performed using the CASAXPS software.

XPS is a technique that can be used to analyze the surface chemistry of a material. It can measure elemental composition including chemical state and electronic state. XPS spectra are obtained by irradiating a material with a beam of X-rays while measuring the kinetic energy (KE) and number of electrons that escape while under high vacuum. The binding energy of the emitted electrons is characteristic of the element from which the photoelectron originated. The position and intensity of the peaks in an energy spectrum provide the desired chemical state and quantitative information. Since the energy of the

x-ray being used with a particular wavelength, hv, is known and the emitted electron's kinetic energies are measured, the electron binding energy (BE) of each of the emitted electrons can be calculated. From the shifts in binding energy the chemical state of elements within the material can be determined. See Equation 18.(*59*)

$$BE = hv - KE \qquad \textbf{Eq. 18}$$

XPS has been used in a number of studies examining the structure-to-property relationship between surface chemistry of non-PGM catalysts and their MEA performance.(*25, 60, 61*) Other studies have used XPS to better understand the degradation of the catalyst layer during MEA testing.(*62*)

For the MEA testing 20wt% of each carbon was added to each of the two catalysts and combined with each Nafion® ionomer ratio. The ink, GDE, and MEA preparation and testing conditions were the same as the samples without carbon addition. All of the polarization curves obtained were compared to determine the optimal performing Nafion® ionomer-to-catalyst ratio and additional carbon content.

Multivariate analysis of the data was done using PLS-Toolbox 5.0 for Matlab. Principal Component Analysis (PCA), using an autoscaling as a preprocessing option (mean centering and scaling to unit variance), was the default method of data analysis. PCA extracts the key mathematical principal components (PC) from a large data matrix by converting it into two smaller matrices that are easier to examine and interpret. The first PC accounts for the largest part of the variance in the data, the second PC accounts for the second-largest part of the variance, and so forth. The results of PCA are usually

displayed as score plots (reflecting the significance of each sample in a principal component), loading plots (reflecting the significance of each variable in a principal component) and bi-plots (showing both samples and variables for two principal components). Bi-plots will be used herein.(*61*)

3.2 OBJECTIVE 2: Chemistry and Morphology of Catalyst and Sprayed Catalyst Layer

The second objective was to better understand the relationship between catalyst and catalyst layer morphology and chemistry and its effect on MEA performance. Thirteen different nitrogen-rich organic precursors were synthesized using the modified SSM described above and screened using MEA testing at 12 psi $(0.8\ bar)_{gauge}$ H_2/O_2 and 30 psi $(2\ bar)_{gauge}$ H_2/air backpressures. From these three were selected for this study; nicarbazin (NCB), sulfaguanidine (SGB), and mebendazole (MBZ). See Figure 13. The materials selection was based on the performance criteria: NCB was one of the worst performing, MBZ was one of the best performing while SGB had performance in between. It should be noted that previous work involving NCB derived catalysts has been published which shows it to have good performance.(*44*, *63*) A not-optimized poor performing formulation of NCB was purposefully chosen as the worst-performing catalyst to better understand the relationship between morphology, chemistry, and performance.

(A) 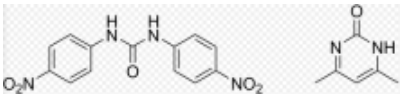 **(B)** 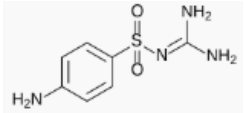 **(C)** 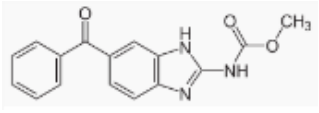

Figure 13. Structures of nitrogen-rich organic precursors. **(A)** NCB **(B)** SGB **(C)** MBZ.

The morphology of the synthesized catlaysts was determined by SEM. A Hitachi S-5200 Nano SEM with an accelerating voltage of 2.0 kV was used. Each image was processed using the ImageJ plug-in called StackReg. The 2D metrics of overall porosity and Euler number were then calculated using an in-house written GUI in Matlab. See below for details. Brunauer–Emmett–Teller (BET) Multipoint surface area of each catalyst was measured using a Micrometrics Gemini system.

The catalysts were made into inks using the same method as stated above but here the inks were sprayed onto a SGL 25BC GDL using a Sono-Tek Exacta-Coat automated spray system delivering 1 mL ink/min. through a 25 kHz ultrasonic nozzle. Catalyst loading was 3.0 mg cm^{-2} ± 0.5. Each catalyst layer was analyzed using an FEI Quanta 3D Dual beam SEM equipped with a field emission gun (FEG). First a protective platinum cap was deposited over the area of interest. Next the focused ion beam (FIB), consisting of Ga^{+} ions accelerated at 30 kV, was used to dig trenches on three sides of the area of interest in order to get a clean view of the catalyst layer. Finally, the FIB was used to slice through the catalyst layer. 160-180 slices were taken every 30 nm. Each slice was imaged using the electron beam at 5.0 kV. The images were then processed using StackReg in ImageJ. The first step of image processing was automatic registration using the "Translation" option. 3D metrics were calculated using an in-house written GUI in Matlab. Roughness was calculated with the original gray scale intensity. For the other 3D metrics, images were thresholded such that solid phase was assigned an intensity value of 1 (white) and pores an intensity value of 0 (black). In this case, solid phase refers

to both the catalyst and ionomer since SEM images do not clearly distinguish between the two phases. See Figure 14.

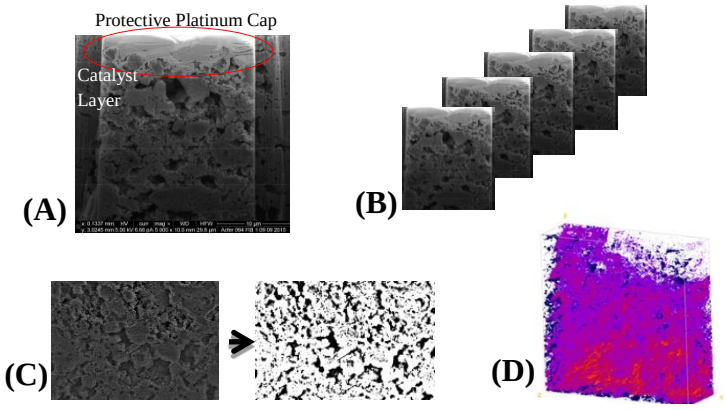

Figure 14. Steps to process images acquired using FIB-SEM. **(A)** FIB dug trenches around the area of interest to get a clean view of the catalyst layer. **(B)** FIB cut slices through the catalyst layer; SEM took an image of each slice. **(C)** Images are processed in the ImageJ plug-in StackReg. **(D)** A visual of the 3D pore volume was reconstructed.

XPS spectra were acquired using the same method described above for objective one. The process for constructing the MEAs was the same as described however polarization curves were acquired at five different backpressures; 12 psi (0.8 bar)$_{gauge}$, 30 psi (2 bar)$_{gauge}$, 12 psi (0.8 bar)$_{gauge}$, 2 psi (0.1 bar)$_{gauge}$ and 60 psi (4 bar)$_{gauge}$. These were taken in H_2/air only.

3.3 OBJECTIVE 3: Integration of Non-PGM HOR Catalysts into Alkaline MEAs

The third objective was to integrate new Ni-based HOR catalysts into alkaline MEAs. For this study the catalyst selected to use was Nickel-Molybdenum-Copper (Ni-Mo-Cu). It was synthesized using a modified SSM. 3 g nickel nitrate hexahydrate ($Ni(NO_3)_2 \cdot 6H_2O$, Sigma Aldrich) was combined with 2 g ammonium molybdate

tetrahydrate ($(NH_4)_6Mo_7O_{24} \cdot 4H_2O$, Sigma Aldrich), hydrous copper (II) nitrate ($Cu(NO_3)_2 \cdot 2.5H_2O$, Sigma Aldrich) and 5 g EHS silica (Cabot). All the materials were mixed together and ball milled for 30 minutes at 350 rpm using an Across International PQ-N04 Planetary ball mill. The mixture was then loaded into a tube furnace and purged with 7% H_2 for 20 minutes. The temperature was increased at a rate of 5 degree/min. to 125 °C, held for 20 minutes, increased further to 235 °C at the same rate, held for 30 minutes, and finally increased to 400 °C and held for 45 minutes. The mixture was allowed to cool down to room temperature before it was ball milled again at 350 rpm for 10 minutes. Next it underwent a second heat treatment. Again the furnace was purged with 7% H_2 for 20 minutes before the temperature was increased to 550 °C at a rate of 10 degree/min. and held for 2 hours. Once the mixture cooled it was passivated with 1% O_2 for 1 hour. Lastly the silica was removed with 7 M KOH for 24 hours until a neutral pH was reached. It was then dried overnight at 85 °C. The BET surface area was measured to be approximately 25 $m^2 g^{-1}$.

Since there is a limited number of published work describing alkaline MEA preparation a reproducible protocol had to be developed. For each parameter optimized the same ink formulation and mixing and spraying technique was used. The ink formulation included 50 mg 40wt% platinum supported on compressed carbon black, 35wt% anion exchange ionomer, and approximately 3 mL IPA. The ink was ball milled at 450 rpm for 1 hour using a 50 mL agate jar with 30 5 mm in diameter agate balls. The ink was then sprayed by hand using a GREX 0.3 mm nozzle TG air brush. For the membrane, ionomer, and membrane exchange optimization the ink was sprayed directly onto the membrane making a catalyst coated membrane (CCM). The membrane was held

against a glass plate heated to 45 °C using a Teflon gasket and the ink sprayed in very light layers alternating vertical and horizontal. Once the first side was sprayed it was allowed to dry before spraying the other side in the same fashion. Each side yielded a loading of 0.3 mg_{Pt} cm^{-2}.

The first set of parameters optimized was the type of membrane and ionomer. The same brand of ionomer and membrane were used together i.e. Tokuyama® AS4 and AS5 ionomer were used with Tokuyama® A201 membrane and fumion® FAA-3 ionomer was used with fumatech® FAA-3 membrane. Initially 35wt% ionomer was used, however later 20wt% was also tried. The second set of parameters optimized was the type of solution used to exchange the membrane into the OH^- form and its duration. Three different solutions were studied: 0.5 M NaOH, 1 M KOH, and 0.5 M KOH. All three were tried at both 24 hours at room temperature followed by 24 hours of a DI water rinse also at room temperature with each solution being changed once. 0.5 M KOH was also tried at 65 °C for one hour followed by a 24 hour DI water rinse. All exchanges and rinses were done in closed containers to prevent as little air as possible interacting with the membranes.

Once the CCMs were finished being rinsed they were assembled into MEAs, still wet, in the following order: 125 µm gasket, 29 BC Sigracet® GDL (facing up), CCM (cathode facing up), another 29 BC Sigracet® GDL (facing down), and another 125 µm gasket. The MEA was cold pressed in a Carver press at 500 psi for 5 minutes, placed in a 5 cm^2 cell with serpentine flow channels, and bolts were tightened to 40 inch-pounds. A Fuel Cell Technologies test station was used to obtain a H_2/O_2 polarization curve for every parameter tried. The anode and cathode gases were heated and fully humidified at

65 °C, and the flow rates were 200 and 250 sccm, respectively. The cell operating temperature was maintained at 60 °C. Polarization curves were acquired potientiostaticly with a 60 second delay before data acquisition at 20 psi $(1.4\ bar)_{gauge}$ backpressure.

It has been shown that CCMs have better performance than GDEs(*64*), however CCMs are very hard to reproduce. Even when sprayed dry using a mask the membranes still tend to wrinkle making reproducing the same CCM difficult. Because of this the final parameter that was optimized was spraying GDEs verses CCMs. The same ink formulation and mixing and spraying technique was used however instead of spraying directly onto the membrane, the ink was sprayed onto a 10 cm^2 29 BC Sigracet® GDL. This was followed by a light top coat of the ionomer. GDEs and their membranes were exchanged separately in 0.5 M KOH at room temperature for 24 hours followed by a 24 hour DI water rinse with each being changed once. The GDEs and their membranes were assembled into MEAs and tested the same as outlined above.

Once a reproducible MEA assembly protocol was established the Ni-Mo-Cu catalyst was integrated into an MEA. For both CCMs and GDEs the Ni-Mo-Cu ink formulation was as follows: 100 mg catalyst, 35wt% AS4 ionomer, and 6 mL IPA. Again the ink was mixed using the ball mill as outlined above. Because the Ni-Mo-Cu agglomerates were bigger than the platinum on carbon black (1-2 μm) a bigger nozzle (0.5 mm) was used. A catalyst loading of 4 mg cm^{-2} was sprayed. The same exchange process, MEA assembly, and testing protocol stated above for CCMs and GDEs was used for the Ni-Mo-Cu anodes.

4. RESULTS

4.1 Objective 1: Optimization of Nafion® Ionomer-to-Catalyst and Additional Carbon Content

MEA performance results were collected in order to determine the optimal amount of Nafion® and additional carbon contents. Adding carbon to the catalyst before being integrated into the MEA is thought to increase the electronic conductivity of the catalyst layer and therefore increase the overall performance of the PEMFC. This is particularly important at higher Nafion® ionomer ratios where excess Nafion® ionomer can get in between the catalyst particles, separating them and breaking the electronic pathway. Here the carbon can act as a bridge reconnecting the pathways. For this study UR and MM nitrogen-rich organic precursors were used (with the purpose to increase the amount of active sites) along with three different Nafion® ionomer ratios; 25wt%, 35wt%, and 45wt%. Three different carbons were tested; Vulcan, KB600, and in-house synthesized CNTs.

Before the carbons were combined with the catalysts and integrated into MEAs their bulk electronic conductivity was first measured using an in-house measurement system. The powder was placed in a Teflon casing with gold electrodes on either end and the electronic conductivity measured under 167 and 1111 psi of pressure. Each carbon was measured individually and each catalyst measured without carbon. Finally 20wt% of each carbon was mixed with both of the catalysts and measured. See Figure 15 for the conductivity measured at 167 psi and Appendix Figure A1 for the conductivity measured at 1111 psi.(*44*)

Catalyst	Conductivity at 167psi (S/cm)
Vulcan	16.6
KB600	6.7
CNT	17.5
UR-no carbon	7.6
UR-Vulcan	9.6
UR-KB600	8.2
UR-CNT	9.4
MM-no carbon	7.2
MM-Vulcan	6.8
MM-KB600	6.1
MM-CNT	7.6

Figure 15. Bulk electronic conductivity measurements taken of UR and MM derived catalysts with and without the addition of carbon.

The UR-derived catalyst had a bulk electronic conductivity of 7.6 S cm^{-2}. The bulk electronic conductivity of the UR-derived catalyst increased with the addition of each carbon. The MM-derived catalyst had a bulk electronic conductivity of 7.2 S cm^{-2}. However, the bulk electronic conductivity of the MM-derived catalyst decreased with the addition of both Vulcan and KB600 and only increased with the addition of the CNTs.

In order to better understand why the MM-derived catalyst's bulk electronic conductivity decreased with the addition of both Vulcan and KB600, XPS spectra was taken. The elemental composition and chemical speciation of carbon was derived for both catalysts with and without 20wt% of each of the three carbons from high resolution C 1s spectra. The data was acquired using a Kratos AXIS DLD Ultra photoelectron spectrometer using monochromatic Al Kα source operating at 225 W. No charge compensation was necessary. Survey spectra were initially acquired at pass energy of 80

eV, followed by high-resolution spectra of Fe 2p, C 1s, O 1s and N 1s at pass energy of 20 eV for all of the samples. See Table 2.(*44*) Data analysis and quantification were performed using the CASAXPS software. A Shirley background was used for quantification and curve fitting of Fe 2p spectra, while a linear background was used C 1s, N 1s and O 1s spectra. Quantification utilized sensitivity factors provided by the manufacturer. A 70% Gaussian/30% Lorentzian line shape was used for the curve-fits.

Sample Identifier	C 1s %	O 1s %	N 1s %	Fe 2p		C gr	C-C/C*	C-N	CxOy
MM	92.0	3.9	3.9	0.09		44.4	24.6	9.9	21.1
MM + Vulcan XC 72R	95.0	2.8	2.1	0.05		57.0	19.1	5.9	17.9
MM + KB 600	92.5	4.3	3.2	0.06		47.4	22.8	7.5	22.3
MM + CNT	93.2	3.6	3.0	0.07		51.8	21.3	7.6	19.3
UR	92.7	3.9	3.3	0.08		42.0	27.5	9.7	20.7
UR + Vulcan XC 72R	94.2	3.5	2.3	0.05		50.7	21.1	7.8	20.4
UR + KB 600	93.1	3.4	3.5	0.06		45.6	25.2	9.5	19.7
UR + CNT	93.3	3.5	3.1	0.07		46.9	25.9	9.5	17.7

Table 2. XPS data taken of UR and MM catalysts with and without the addition of carbon.

Out of all the carbon additives, only with the addition of Vulcan does the overall elemental composition of the catalysts change by introducing larger amounts of carbon at the expense of nitrogen and iron. The role of nitrogen for the ORR active sites was discussed above. Importantly, the overall nitrogen and iron speciation is not affected by the addition of carbon (not shown). The speciation of carbon, on the other hand, changes significantly after carbon additives were introduction. None of the carbon additives introduced carbon oxides, while graphitic content is increased for all carbon additives. KB600 has a smallest effect on carbon chemistry introducing slightly more graphitic

carbon into the catalyst. Vulcan introduced the highest amount of graphitic carbon and lowered the amount of C-N centers significantly. CNTs had a similar effect causing an increase of graphitic carbon, decreasing the amount of surface oxides and, thus decreasing wettability of the catalyst.

The final step in this study was to test each of the two catalysts with all three Nafion® ionomer ratios with and without 20wt% of each of the three carbons in MEA configurations. First both catalysts were tested with each Nafion® ionomer ratio without carbon in both 12 psi $(0.8\ bar)_{gauge}$ and 30 psi $(2\ bar)_{gauge}$ $backpressure_{(gauge)}$ H_2/air. See Figures 16 (A), (B), (C) and (D).(*44*)

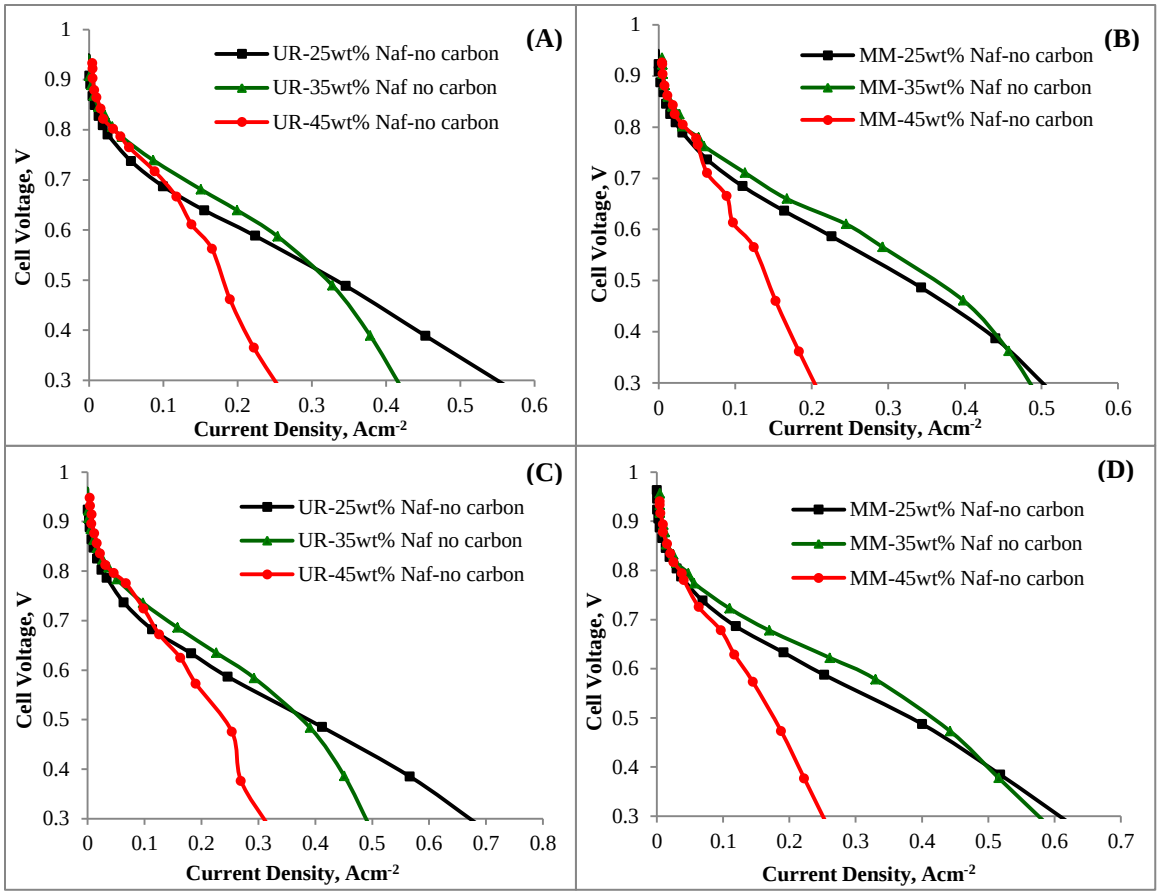

Figure 16. Polarization curves for both catalysts with 25wt%, 35wt%, and 45wt% Nafion® ionomer without additional carbon taken in H_2/air **(A)** MM-derived catalyst at 12 $(0.8\ bar)_{gauge}$ psi backpressure **(B)** UR-derived catalyst at 12 $(0.8\ bar)_{gauge}$ psi backpressure **(C)** MM-derived catalyst taken at 30 $(2\ bar)_{gauge}$ psi backpressure **(D)** UR-derived catalyst at 30 $(2\ bar)_{gauge}$ psi backpressure.

Finally both catalysts were tested with each Nafion® ionomer ratio with 20wt% Vulcan, KB600, and CNTs in both 12 psi $(0.8\ bar)_{gauge}$ and 30 psi $(2\ bar)_{gauge}$ backpressure H_2/air. See Figures 17 (A), (B), (C) and (D).(*44*) Separate polarization curves for each additional carbon with each catalyst and Nafion® ionomer ratio are Appendix figures A2, A3, and A4.(*44*)

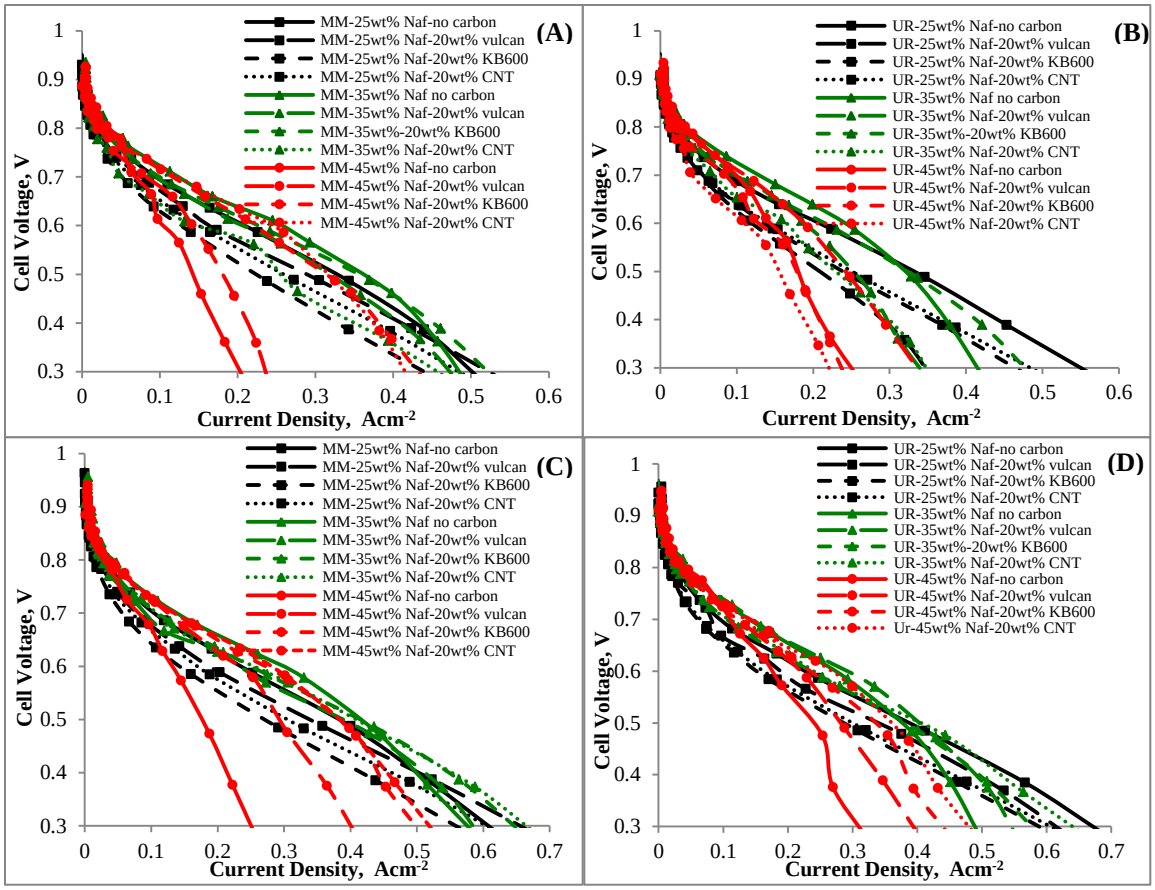

Figure 17. Polarization curves for both catalysts with 25wt%, 35wt%, and 45wt% Nafion® ionomer with 20wt% Vulcan, KB600, and CNTs taken in H_2/air **(A)** MM-derived catalyst at 12 $(0.8\ bar)_{gauge}$ psi backpressure **(B)** UR-derived catalyst at 12 $(0.8\ bar)_{gauge}$ psi backpressure **(C)** MM-derived catalyst taken at 30 $(2\ bar)_{gauge}$ psi **(D)** UR-derived catalyst at 30 $(2\ bar)_{gauge}$ psi backpressure.

The best performance with reguards to Nafion® ionomer ratio for both catalysts without additional carbon at both backpressures was as follows: in the kinetic region (0.8 V) 45wt% Nafion® ionomer was best for both, in the ohmic region (0.6 V) 35wt% was best for both, and in the transport region (0.4 V) 25wt% Nafion® ionomer was best for UR-derived catalysts and 35wt% was best for MM-derived catalysts.

At 12 psi (0.8 bar)$_{gauge}$ backpressure the addition of each carbon improved the overall performance when 45wt% Nafion® ionomer was used for both catalysts, however for 25wt% and 35wt% each additional carbon decreased the overall performance of both catalysts. At 30 psi (2 bar)$_{gauge}$ backpressure the addition of each carbon improved the overall performance of both catalysts with 45wt% and 35wt% Nafion® ionomer, however for 25wt% each additional carbon decreased the overall performance of both catalysts.

Table 3 is a summary of the measured current densities at 0.8 V, 0.6 V and 0.4 V for each MEA tested at both backpressures. Figure 18 shows the resulting bi-plots when principal component analysis was applied to the data from Table 3.(*44*) Bi-plots were used because they provide a more instructive visualization of the groups of samples that are similar to each other and variables that are the most or least important for a specific sample group. Variables and samples that were highly correlated are in the same region on the bi-plot.

Y-axis separates the plot into principal component 1 representing transport region on the left and kinetic region on the right. Principal component 2 separates the plot along the x-axis into the top half representing the better performing samples and the bottom half the worse performing samples at all potentials. The resulting four quadrants provide insight into correlations between the variables. Quadrant I indicated that higher Nafion® content was important for the kinetic region, specifically the MM samples with added KB600 and CNTs. Also both the UR and MM samples without carbon showed good performance in the kinetic region when 35wt% Nafion® was used. The correlation between the good performance in the ohmic region (0.6 V) and 35wt% Nafion® can be seen in Quadrants I and II. Quadrant II indicated that a higher Nafion® content should be

avoided for better performance in the transport region. Here both the UR and MM samples without carbon additives showed good performance in the transport region when 25wt% Nafion® ionomer was used. Quadrant III pointed to the fact that all samples with added carbon and lowest wt% Nafion® ionomer had worse performance than samples with added carbon and higher Nafion® ionomer contents. Again this fit the hypothesis that only when higher amounts of Nafion® were used is adding carbon effective in increasing performance. Finally, Quadrant IV indicated that, in general, all samples with 45wt% Nafion® ionomer had the worst performance. The optimal ink configurations resulting in the balance between kinetic and transport regions are inks made based on both MM and UR catalysts with 35wt% Nafion® ionomer and carbon free. As XPS results above have shown, KB600 had the smallest effect on carbon chemistry among the three carbon additives used, while CNTs and Vulcan introduced too much graphitic carbon changing the hydrophobic properties of the catalysts substantially and resulting in a decrease in overall cell performance.

Catalyst	Nafion content (wt%)	Carbon Type (20wt%)	Current Density (A cm^{-2}) 12 $psi_{(gauge)}$				Current Density (A cm^{-2}) 30 $psi_{(gauge)}$		
			0.8 V	**0.6 V**	**0.4 V**		**0.8 V**	**0.6 V**	**0.4 V**
Fe-NCB with UR	25	no carbon	0.021	0.210	0.440		0.026	0.225	0.540
Fe-NCB with UR	25	Vulcan	0.017	0.120	0.290		0.029	0.188	0.485
Fe-NCB with UR	25	KB600	0.013	0.135	0.355		0.016	0.150	0.440
Fe-NCB with UR	25	CNT	0.013	0.141	0.365		0.017	0.165	0.460
Fe-NCB with UR	35	no carbon	0.035	0.242	0.375		0.041	0.275	0.441
Fe-NCB with UR	35	Vulcan	0.025	0.088	0.295		0.037	0.290	0.485
Fe-NCB with UR	35	KB600	0.024	0.215	0.410		0.028	0.235	0.485
Fe-NCB with UR	35	CNT	0.018	0.165	0.300		0.026	0.240	0.530
Fe-NCB with UR	45	no carbon	0.034	0.144	0.210		0.042	0.175	0.265
Fe-NCB with UR	45	Vulcan	0.029	0.088	0.290		0.034	0.220	0.340
Fe-NCB with UR	45	KB600	0.022	0.128	0.210		0.036	0.235	0.440
Fe-NCB with UR	45	CNT	0.013	0.110	0.188		0.034	0.270	0.420
Fe-NCB with MM	25	no carbon	0.026	0.210	0.430		0.031	0.235	0.498
Fe-NCB with MM	25	Vulcan	0.018	0.163	0.410		0.021	0.185	0.500
Fe-NCB with MM	25	KB600	0.012	0.126	0.325		0.015	0.141	0.270
Fe-NCB with MM	25	CNT	0.015	0.150	0.378		0.018	0.170	0.460
Fe-NCB with MM	35	no carbon	0.032	0.257	0.435		0.043	0.300	0.498
Fe-NCB with MM	35	Vulcan	0.022	0.206	0.410		0.026	0.235	0.510
Fe-NCB with MM	35	KB600	0.025	0.226	0.450		0.029	0.250	0.548
Fe-NCB with MM	35	CNT	0.015	0.148	0.350		0.030	0.255	0.548
Fe-NCB with MM	45	no carbon	0.034	0.105	0.170		0.035	0.130	0.213
Fe-NCB with MM	45	Vulcan	0.018	0.141	0.212		0.037	0.235	0.350
Fe-NCB with MM	45	KB600	0.029	0.223	0.380		0.037	0.270	0.440
Fe-NCB with MM	45	CNT	0.027	0.245	0.376		0.033	0.280	0.455

Table 3. Summary of the measured current densities at 0.8 V, 0.6 V and 0.4 V for each MEA tested at both 12 psi $(0.8\ bar)_{gauge}$ and 30 psi $(2\ bar)_{gauge}$ H_2/air backpressure.

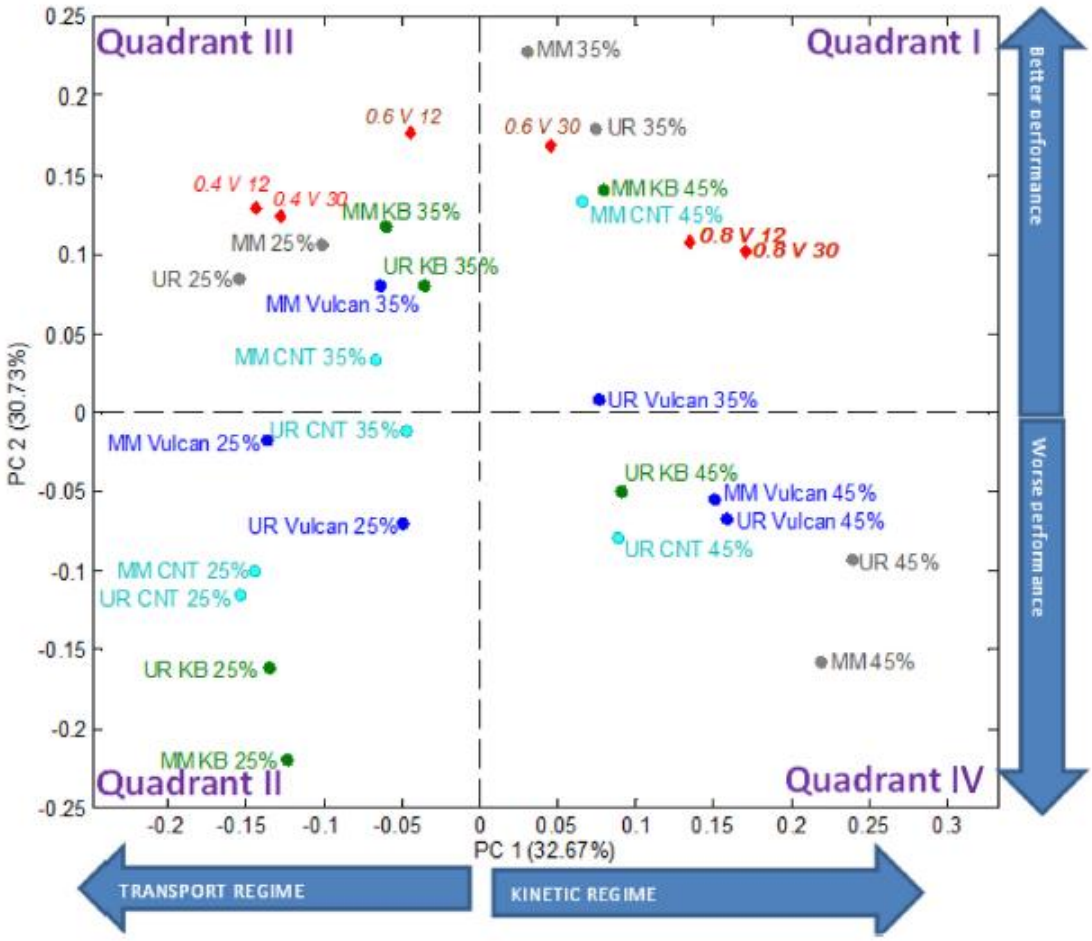

Figure 18. Bi-plots provide a more instructive visualization of the groups of samples that are similar to each other and variables that are the most or least important for a specific sample group.

For both MM and UR derived catalysts when tested at 12 psi $(0.8\ \text{bar})_{\text{gauge}}$ backpressure all three additional carbon types improved performance for MEAs with 45wt% Nafion® ionomer, while hindering performance in the MEAs made with lower ratios of Nafion® ionomer. This was not necessarily the case when all samples were tested at 30 psi $(2\ \text{bar})_{(\text{gauge})}$ backpressure. This supports the hypothesis that when higher ratios of Nafion® ionomer was used, the performance was poor due to transport hindrance and

distorted electronic pathways, adding carbon can enhance the performance. However at lower Nafion® ionomer ratios adding additional carbon lowered overall performance. From these results it was concluded that the best performing catalyst layers have a lower Nafion® ionomer ratio and no additional carbon. Additional carbon was only beneficial when higher amounts of Nafion® ionomer were used.

4.2 OBJECTIVE 2: Chemistry and Morphology of Catalyst and Sprayed Catalyst Layer

Polarization curves were used to screen thirteen different nitrogen-rich organic precursors. The resulting catalytic performance was measured potentiostaticlly in both 30 psi (2 bar)$_{gauge}$ H_2/air and 12 psi (0.8 bar)$_{gauge}$ H_2/O_2 backpressures and the resulting polarization curves plotted. See Figure 19 (A) and (B).(*65*)

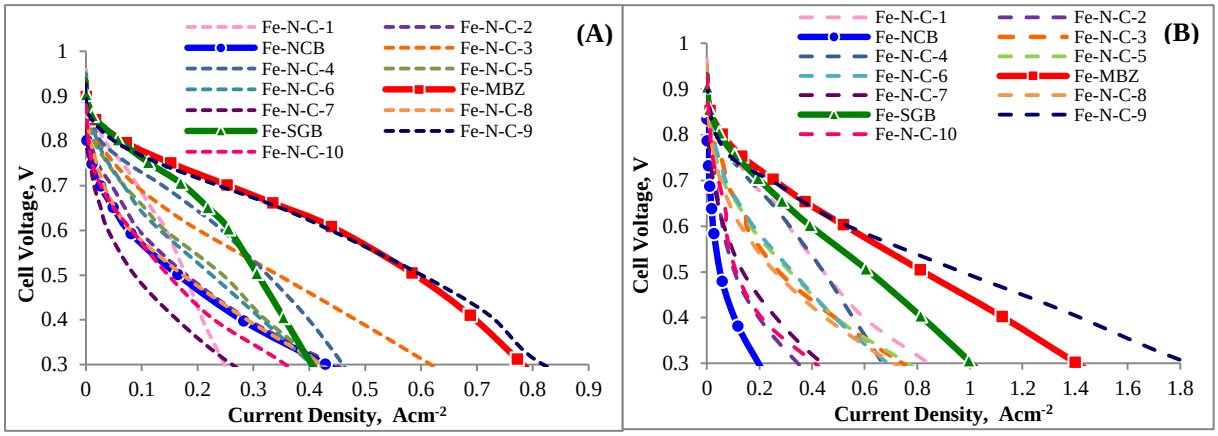

Figure 19. Polarization curves collected from MEA screening of organic precursors **(A)** 30 psi (2 bar)$_{gauge}$ H_2/air **(B)** 12 psi (0.8 bar)$_{gauge}$ H_2/O_2.

Three precursors were selected to study further; MBZ, SGB, and NCB due to their high, medium and low performance.

First the morphology of the synthesized catalysts were analyzed by SEM. The material had a well-developed porous structure formed by two mechanisms: (1) the removal of silica support and (2) the decomposition of organic molecules. See Figure 20.(*65*) The removal of the silica template left the catalysts with a surface area between 500 and 650 $m^2 g^{-1}$ as measured by BET, with pores of ~50-70 nm. Such porous structure was beneficial for effective transport of oxygen to active sites as well as for water management.

From the SEM images, the 2D metrics of overall porosity and Euler number were calculated for each catalyst. Porosity is the ratio of void volume (pores) to total volume. Euler number is the total number of objects (solid phase) minus the total number of pores in those objects. Pore connectivity is determined by the number of connected pixels representing pores.(*66*) The lower the Euler number, the more connected the pores present within the solid phase. Figure 21 summarizes the 2D metrics for all three catalysts.(*65*) Fe-NCB has the highest overall porosity while Fe-MBZ has the lowest. However, Fe-MBZ has the lowest Euler number while Fe-NCB has the highest. This indicates that Fe-MBZ has the best pore connectivity.

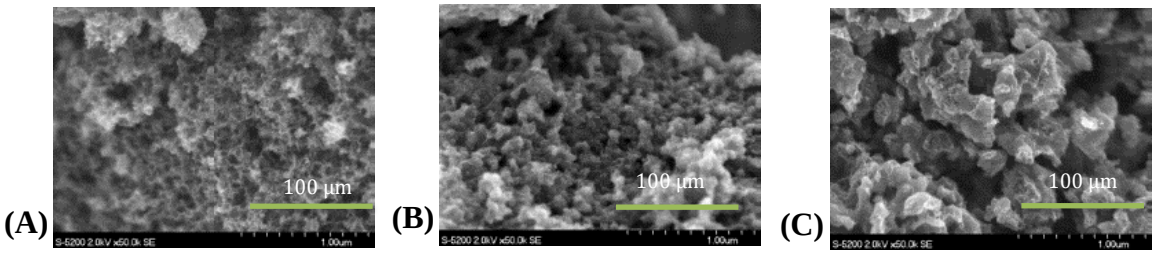

Figure 20. SEM images of catalysts prepared by the SSM. **(A)** Fe-NCB **(B)** Fe-SGB **(C)** Fe-MBZ.

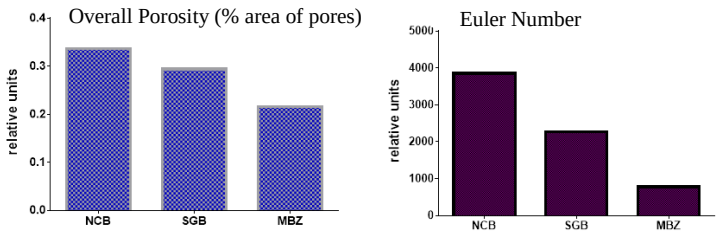

Figure 21. Summary of 2D metrics.

The morphology of the catalyst layers was examined using FIB-SEM. A 2D image of a slice from each catalyst layer can be seen in Figure 22.(*65*) As discussed in the research design section, 160-180 slices were acquired for each catalyst layer, which were then registered to create a 3D volume of the material. First, a 3D visualization of pores in each catalyst layer was reconstructed. See Figure 23.(*65*) The pores are indicated in red. Fe-NCB had a higher intensity of red meaning the pores are bigger. However the red clustered together and not homogeneously spread throughout the catalyst layer indicated lower pore connectivity. Fe-SGB showed less red intensity indicating smaller pores. However the red is uniformly spread throughout the catalyst layer meaning better pore connectivity. Fe-MBZ had a higher intensity of red spread almost throughout the whole catalyst layer. This means that Fe-MBZ was overall more homogenous and had good pore connectivity.

From the processed images, 3D metrics were calculated. See Figure 24.(*65*) First, 3D roughness or the overall image heterogeneity was calculated. This was based on the greyscale images before thresholding. Here Fe-NCB had the highest roughness followed by Fe-SGB while Fe-MBZ had the lowest. This means that overall Fe-MBZ was more homogeneous. Next solid phase size and pore size was calculated from the thresholded

images. Solid phase size was measured as the average number of consecutive pixels representing the solid phase (pixels with an intensity value of 1) in a given direction. Here, Fe-NCB had the highest solid phase size followed by Fe-SGB while Fe-MBZ had the lowest solid phase size. The metrics representative of pore size were calculated as an average diffusion distance, or the average distance from a solid phase pixel to the nearest void pixel in the image (pore having an intensity value of 0). This measured the closeness of solid phase clusters or the pore size between these clusters. (*67*, *68*) Here again, Fe-NCB had the highest pore size followed by Fe-SGB while Fe-MBZ had the lowest. Lastly, Euler number was calculated from the thresholded images. As mentioned, the lower the Euler number, the more connected the pores are throughout the catalyst layer. Here Fe-NCB had an Euler number around 0 while both Fe-SGB and Fe-MBZ had Euler numbers that were negative. This indicated that both Fe-SGB and Fe-MBZ had higher pore connectivity than Fe-NCB. These metrics agree with the conclusions drawn from the 3D reconstructed pore volume in Figure 23.

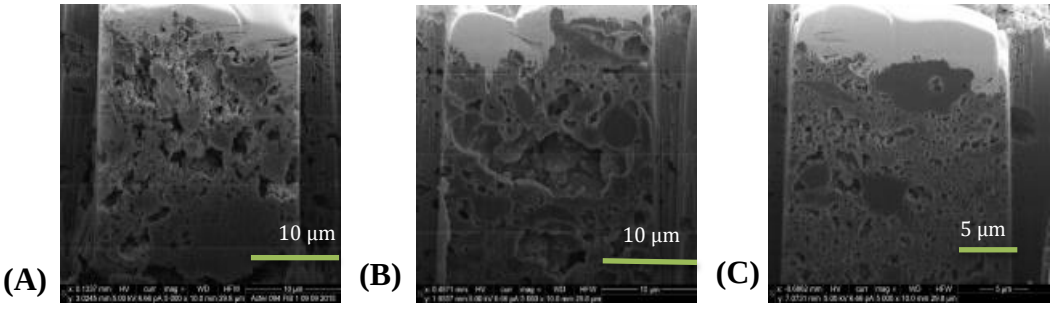

Figure 22. 2D FIB-SEM images of each of the catalyst layers that were sprayed onto GDLs. **(A)** Fe-NCB **(B)** Fe-SGB **(C)** Fe-MBZ.

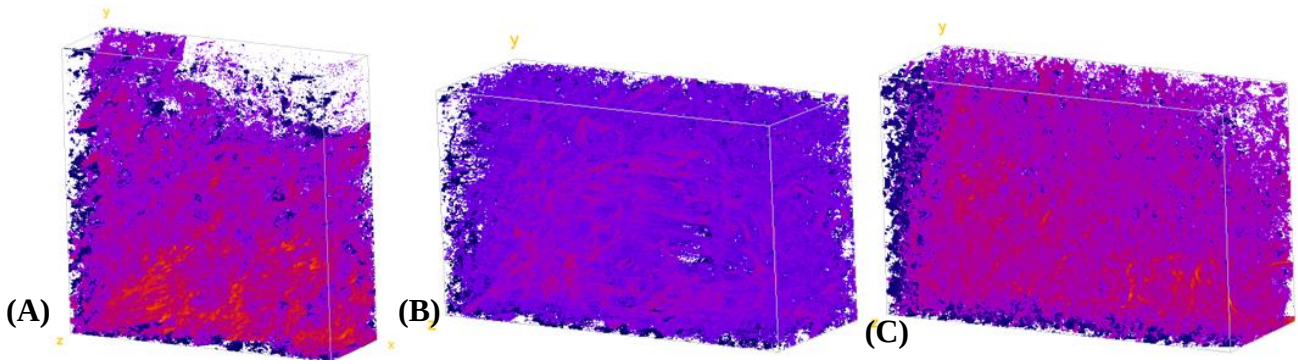

Figure 23. 3D reconstruction of catalyst layer pore volume, indicated in red. **(A)** Fe-NCB **(B)** Fe-SGB **(C)** Fe-MBZ.

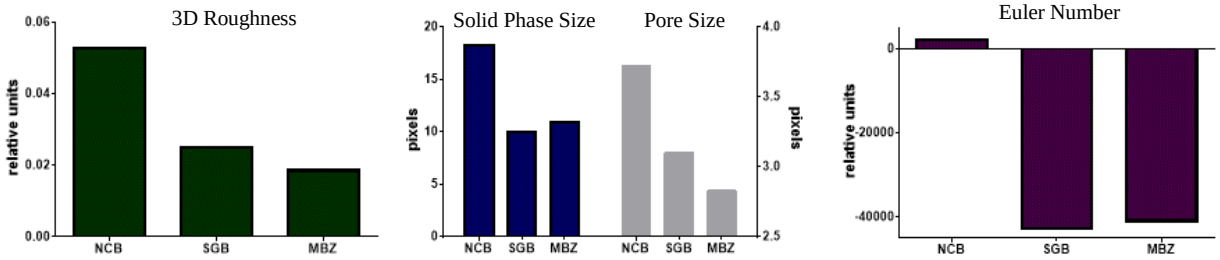

Figure 24. Summary of catalyst layer 3D metrics calculated from FIB-SEM images.

The catalysts' performance was evaluated using MEAs. The performance was compared using polarization curves. As mentioned above, each MEA was tested at 5 different pressures. Since the focus of this study was the catalyst layer, the interest was in as close to beginning of life performance as possible. In this case, that is the first polarization curve at 12 psi (0.8 bar)$_{gauge}$ backpressure. As can be seen in Figure 25, Fe-SGB and Fe-MBZ have the same performance at 0.8 V, the kinetic region, however, Fe-NCB performed significantly worse. At 0.6 V, in the ohmic region, Fe-SGB was only slightly worse than Fe-MBZ but again Fe-NCB was significantly worse. Finally at 0.4 V, in the transport region, Fe-MBZ had the best performance, followed by Fe-SGB. Fe-

NCB's performance was almost an order of magnitude worse than Fe-MBZ. As shown in the above section, one possible reason for Fe-NCB's poor transport performance is the lack of pore connectivity.(*65*)

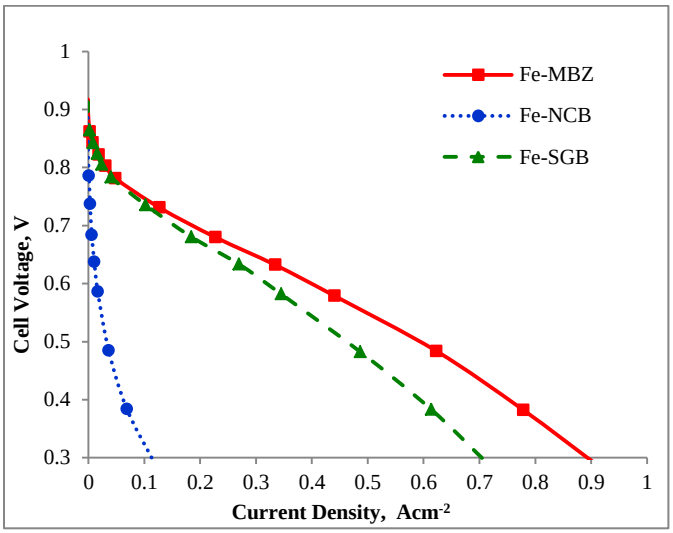

Figure 25. First 12 psi (0.8 bar)$_{gauge}$ backpressure H_2/air polarization curves were used to measure beginning of life performance.

There were two types of mass transport losses that can lead to poor MEA performance, gaseous transport, and liquid transport. Liquid transport refers to both water and ionomer that can potentially block pores. One way to determine what type of transport loss was occurring within the catalyst layer was testing the MEA in both air and oxygen. Oxygen has a higher activity than air, if the transport limitation is gaseous then oxygen will perform better, however if the transport limitation is liquid, then pores and active sites are being blocked, therefore the performance for both gases will be the same. Figure 26 (A), 27 (A), and 28 (A) are Fe-MBZ, Fe-SGB, and Fe-NCB tested in 12 psi (0.8 bar)$_{gauge}$ backpressure H_2/O_2 and 60 psi (4 bar) $_{gauge}$ backpressure H_2/Air respectively.(*65*) These pressures were chosen so that the same amount of oxygen was

present in each case. For Fe-MBZ and Fe-SGB the solid line, O_2, has better performance than the dotted line, air. This means that the transport performance is gaseous limited. However for Fe-NCB air and oxygen performed the same which indicated liquid transport loss.

Another method to determine the type of transport limitation present was to compare the polarization curves of the same MEA tested at different backpressures, in this case in H_2/air. Figure 26 (B), 27 (B), and 28 (B) were Fe-MBZ, Fe-SGB, and Fe-NCB tested at the five pressures listed above.(*65*) As can be seen, performance increased as pressure increased for Fe-MBZ and Fe-SGB. This means that as more gas was pushed through the catalyst layer the performance improved. This again indicated that performance was gaseous transport limited. If the performance was liquid transport limited all pressures would have had the same performance due to pore and active site blockage as can be seen from Figure 28 (B), Fe-NCB.

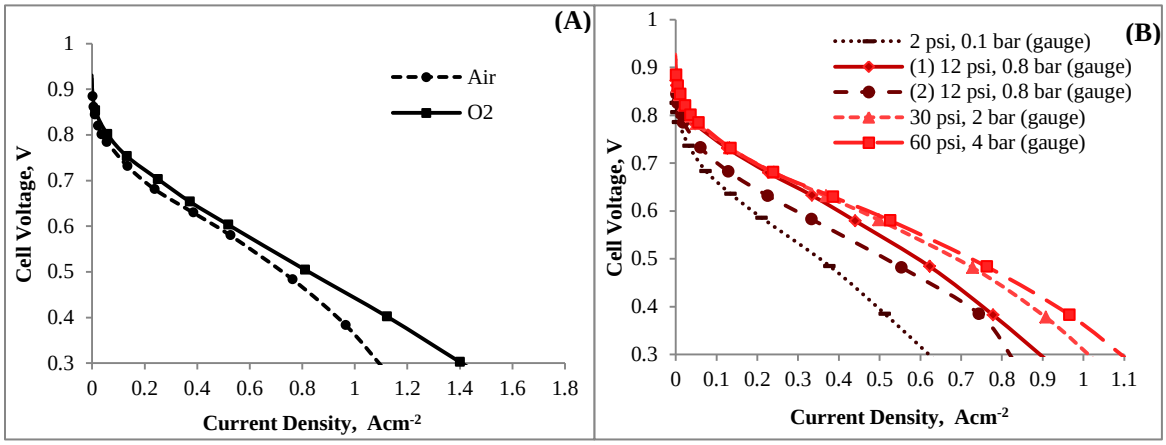

Figure 26. **(A)** Fe-MBZ tested in both 60 psi (4 bar)$_{gauge}$ backpressure H_2/air and 12 psi (0.8 bar)$_{gauge}$ backpressure H_2/O_2. **(B)** Fe-MBZ tested in H_2/air at five different backpressures.

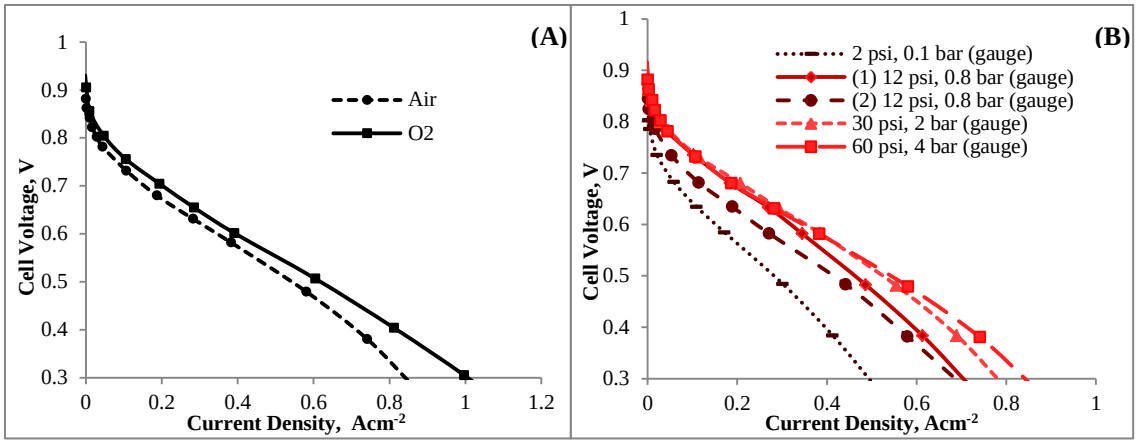

Figure 27. **(A)** Fe-SGB tested in both 60 psi (4 bar)$_{gauge}$ backpressure H_2/air and 12 psi (0.8 bar)$_{gauge}$ backpressure H_2/O_2. **(B)** Fe-SGB tested in H_2/air at five different backpressures.

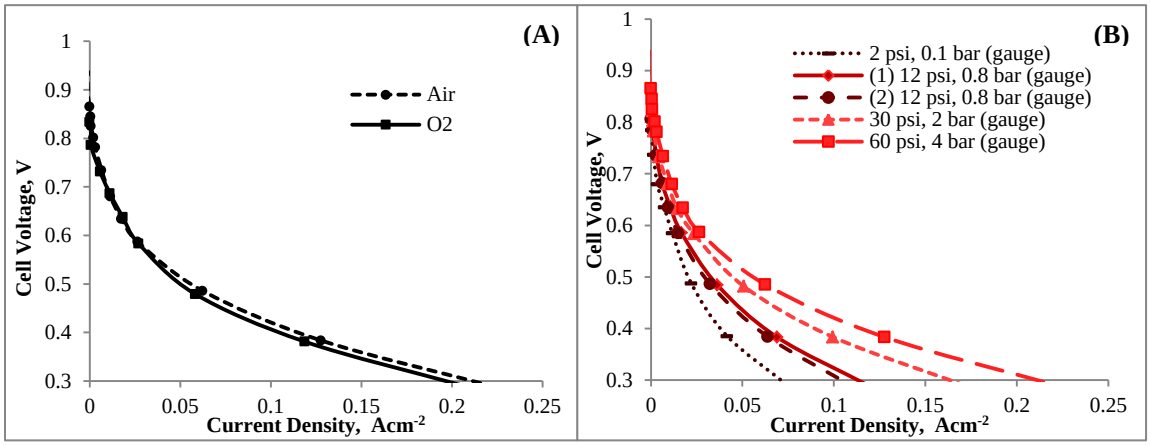

Figure 28. **(A)** Fe-NCB tested in both 60 psi (4 bar)$_{gauge}$ backpressure H_2/air and 12 psi (0.8 bar)$_{gauge}$ backpressure H_2/O_2. **(B)** Fe-NCB tested in H_2/air at five different backpressures.

Table 4 shows the elemental composition and nitrogen speciation of catalysts as determined by XPS.(*65*) Fe-MBZ had the highest amount of Fe detected while Fe-NCB had the lowest amount of both N and Fe detected. This could be one of the reasons for the

poor performance of Fe-NCB, it had fewer active sites than the other two catalysts. Six types of nitrogen can be separated from high resolution spectra. See Figure 26.(*65*) Going from low to high binding energy these types of nitrogen were – imine, pyridinic, nitrogen coordinated to the metal, pyrrolic, quaternary or protonated N and graphitic nitrogen. In previously published reports, higher amounts of nitrogen coordinated to metal were correlated with better ORR activity. (*69, 70*) This is also seen in this study where Fe-MBZ had the most nitrogen coordinated to metals and Fe-NCB had the least. The species contributing to higher binding energy range such as pyrrolic, protonated and graphitic N results in preferential two electron reduction of oxygen to hydrogen peroxide. (*69, 71, 72*) Fe-NCB powder had the highest amount of pyrrolic nitrogen and lowest amount of nitrogen coordinated to the metal. Fe-MBZ, on the other hand, had the highest amount of beneficial Fe-N_x centers and lowest amount of pyrrolic nitrogen among the three samples.

Sample Identifier	C 1s %	O 1s %	N 1s %	Fe 2p		
Fe-MBZ powder	92.1	3.9	3.7	0.30		
Fe-SGB powder	90.2	5.6	3.9	0.27		
Fe-NCB powder	92.7	3.8	3.3	0.15		
	Imine	Pyridine	Nx-Me	N pyrrole	N qua	N gr
Fe-MBZ powder	10.1	22.6	15.5	29.7	17.7	4.3
Fe-SGB powder	7.7	21.1	13.6	32.3	19.2	6.0
Fe-NCB powder	7.7	24.8	10.4	38.3	11.6	7.0

Table 4. Elemental composition and nitrogen speciation of catalysts as determined by XPS.

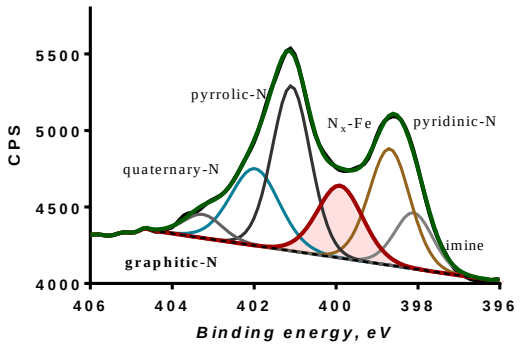

Figure 29. Types of nitrogen that can be separated from high resolution spectra for Fe-MBZ.

4.3 OBJECTIVE 3: Integration of Non-PGM HOR Catalysts into Alkaline MEAs

Polarization curves were collected in order to determine the best procedure for making alkaline MEAs. The steps taken to establish a reproducible procedure were all done using platinum supported on carbon for both electrodes. Once a procedure was established polarization curves were then used to evaluate MEAs made with Ni-Mo-Cu HOR catalysts. The first parameters optimized were the membrane and ionomer type and amount. Two commercially available membranes were tried, Tokuyama® A201 and fumatech® FAA-3. Tokuyama® performed significantly better. See Figure 30 (A). One of the issues experienced with the fumatech® membrane was substantial swelling which might account for the poor transport performance. Next the type of Tokuyama® ionomer used was optimized, AS4 verses AS5. AS4 performed better. See Figure 30 (B). AS5 is the newer generation of Tokuyama® ionomer however the structure is propriety so it is not possible to evaluate performance based on structure. Then the amount of AS4 ionomer was optimized; 20wt% and 35wt%. 35wt% performed significantly better. See Figure 30 (C). This follows the same trend seen in Figure 16, that is 35wt% is the best

performing while anything less than that performed worse. The second set of parameters optimized was exchange solution and duration. The best performing was 0.5 M KOH at room temperature for 24 hours. There wasn't much difference when 1.0 M KOH at room temperature for 24 hours was used. When the solution was switched to 1.0 M NaOH at room temperature for 24 hours it performed slightly worse. A shorten exchange time and elevated temperature using 0.5 M KOH at 65 °C for 4 hours performed the worst. This could be because it was not enough time, even with the raised temperature, for the membrane to fully exchange. See Figure 30 (D).

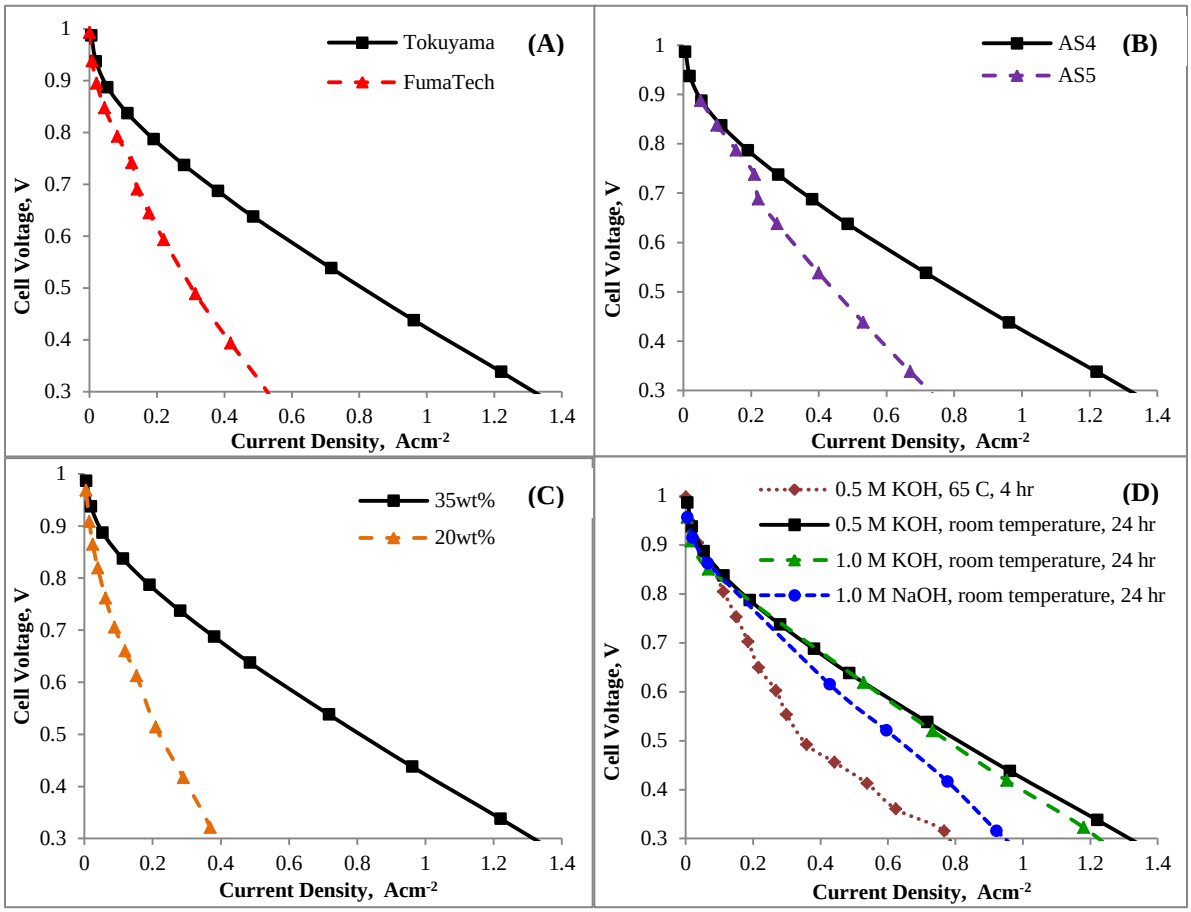

Figure 30. Optimized parameters for developing a reproducible alkaline MEA assembly procedure. **(A)** Commercial membrane **(B)** Ionomer **(C)** Ionomer Amount **(D)** Exchange solution and duration.

The alkaline MEA assembly procedure established to use for all further MEAs was Tokuyama® A201 membrane with 35wt% Tokuyama® AS4 ionomer exchanged in 0.5 M KOH at room temperature for 24 hours followed by a 24 hour DI water rinse also at room temperature. Both the KOH solution and the DI water were changed once during the 24 hour periods.

The final parameter studied was the type of MEA, CCM vs. GDE. As previously mentioned, CCMs usually outperform GDEs and this trend can be seen in Figure 31. Figure 31 (A) used platinum supported on carbon for both electrodes. One of the possible reasons for the performance discrepancy could be the catalyst layer-membrane interface. With CCMs the interface is virtually seamless however with GDEs there may not be good contact between the membrane and the catalyst layer. The final step for this objective was to integrate Ni-Mo-Cu HOR catalysts into the alkaline MEA with a loading of 4 mg cm^{-2}. First a CCM was made followed by a GDE. See Figure 31 (B). The CCM had extremely low performance whereas the GDE had no performance. Both show some OCV however very little or nonexistent current. A lack of current indicates little to no electron movement.

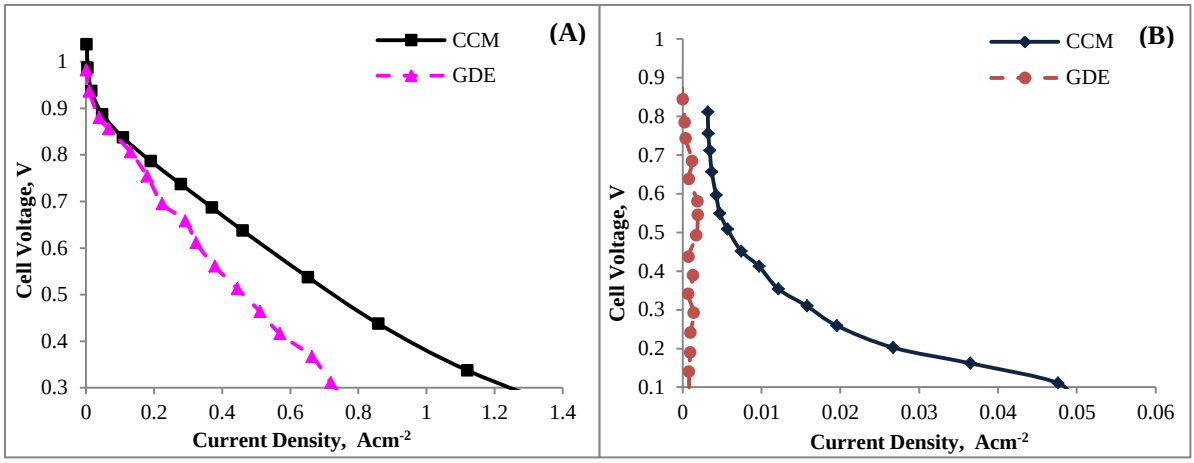

Figure 31. (A) CCM vs. GDE where both electrodes were platinum supported on carbon. **(B)** CCM vs. GDE using Ni-Mo-Cu HOR catalyst.

5. CONCLUSIONS AND SIGNIFICANCE

First, optimized catalyst layer composition is unique for each catalyst. This was seen in the performance differences between the two catalysts when 25wt% and 35wt% Nafion® ionomer was used. In general higher amounts of Nafion® ionomer lead to poor overall performance most likely do to pore and active site blocking and loss of electronic conductivity. This can be corrected with the addition of carbon. For every MEA made with 45wt% Nafion® ionomer the performance improved with each carbon addition. This was seen at both pressures tested. At the higher pressure tested additional carbon also improved the overall performance when 35wt% Nafion® ionomer was used. Without additional carbon when lower amounts of Nafion® ionomer were compared the higher content was slightly better confirming the theory that an increase in Nafion® ionomer increases ionic conductivity and therefore increases overall performance.

The best indicator of good transport within a catalyst and its sprayed layer is the pore connectivity. Furthermore transport losses are dominated by gaseous transport for

both Fe-MBZ and Fe-SGB. However, Fe-NCB was liquid transport limited, possibly due to low pore connectivity and minimal access to the active sites. Catalyst chemistry is also a good indicator of performance. Higher amounts of both nitrogen and metal, particularly nitrogen coordinated to metal, lead to more active sites and better overall performance. Species that contribute to higher binding energies generally indicated lower overall performance.

A successful protocol for making alkaline MEAs has been established and is comparable to what has been reported in the literature.

The significance of the work presented is twofold. First, there are multiple factors that go into making non-PGM catalysts a realistic platinum replacement. This work shows the importance of optimizing both the catalyst layer composition and its morphology in order to get the most performance out of non-PGM catalysts and is crucial in developing governing equations for non-PGM polarization curves. Second, and more importantly, this work shows significant progress in making alkaline MEAs. The protocol established for constructing and exchanging alkaline MEAs with platinum supported on carbon electrodes is equal to or exceeds what have been reported in the literature. To the best of the author's knowledge this was the first time MEA data for Ni-Mo-Cu HOR catalysts was collected successfully. This represents a huge push for making AEMFCs a viable fuel cell option.

6. PATENTS

A. Serov, S. Kabir, **S. Stariha**, P. Atanassov, *Method of Preparation of Nano-Sized Materials and Apparatus Incorporating the Same*. 2015: United States of America. International publication number WO 2015/175656 A1

7. PUBLICATIONS IN PEER REVIEWED JOURNALS

S. Stariha, K. Artyushkova, A. Serov, P. Atanassov, "Non-PGM Membrane Electrode Assemblies: Optimization for Performance" International Journal of Hydrogen Energy Volume 40, pages 14676-14682, 2015.

S. Stariha, K. Artyushkova, M. J. Workman, A. Serov, S. Mckinney, B. Halevi, P. Atanassov, "Non-PGM Fe-N-C Catalysts for Oxygen Reduction Reaction: Catalyst Layer Design" Submitted to Journal of Power Sources.

C. Santoro, A. Serov, C. W. Narvaez Villarrubia, **S. Stariha**, S. Babanova, A. J. Schuler, K. Artyushkova, P. Atanassov, "Double-Chamber Microbial Fuel Cell with a Non-Platinum-Group Metal Fe–N–C Cathode Catalyst" ChemSusChem Volume 8, Issue 5, pages 828–834, 2015

A. Serov , K. Artyushkova, N. I. Andersen, **S. Stariha,** P. Atanassov, "Original Mechanochemical Synthesis of Non-Platinum Group Metals Oxygen Reduction Reaction Catalysts Assisted by Sacrificial Support Method" Electrochimica Acta Volume 179, pages 154-160, 2015.

C. Santoro, A. Serov, C. W. Narvaez Villarrubia, **S. Stariha**, S. Babanova, K. Artyushkova, A. J. Schuler, P. Atanassov, "High catalytic activity and pollutants resistivity using Fe-AAPyr cathode catalyst for microbial fuel cell application. *Scientific Reports* 5, DOI: 10.1038/srep16596, 2015.

T. Reshetenko, A. Serov, **S. Stariha**, I. Matanovic, K. Artyushkova, J. St-Pierre, P. Atanassov, "Influence of Air-Borne Contaminants on Performance of non-PGM ORR Catalysts" Submitted to Journal of Power Sources.

8. PRESENTATIONS PUBLISHED AS ABSTRACTS

S. Stariha, K. Artyushkova, A. Serov, B. Halevi, P. Atanassov, "Non-PGM Fe-N-C Catalysts for Oxygen Reduction Reaction in PEMFCs: MEA Design". Presented at the 228th ECS meeting in Phoenix, Arizona as a 20 minutes talk. October 2015.

S. Stariha, K. Artyushkova, A. Serov, B. Halevi, P. Atanassov, "Non-PGM Membrane Electrode Assemblies: Optimization for Performance". Presented at the 226th ECS meeting in Cancun, Mexico as a 20 minutes talk. October 2014.

9. REFERENCES

1. J. M. Song, S. Y. Cha, W. M. Lee, Optimal composition of polymer electrolyte fuel cell electrodes determined by the AC impedance method. *Journal of Power Sources* **94**, 78-84 (2001).
2. M. L. Perry, T. F. Fuller, A Historical Perspective of Fuel Cell Technology in the 20th Century. *Journal of the Electrochemical Society* **149**, S59-S67 (2002).
3. J. R. Varcoe *et al.*, Anion-exchange membranes in electrochemical energy systems†. *Energy Environ. Sci.* **7**, 3135-3191 (2014).
4. G. Merle, M. Wessling, K. Nijmeijer, Anion exchange membranes for alkaline fuel cells: A review. *Journal of Membrane Science* **377**, 1-35 (2011).
5. G. F. McLean, T. Niet, S. Prince-Richard, N. Djilali, An assessment of alkaline fuel cell technology. *Int. J. Hydrog. Energy* **27**, 507-526 (2002).
6. W. Sheng *et al.*, Non-precious metal electrocatalysts with high activity for hydrogen oxidation reaction in alkaline electrolytes. *Energy Environ. Sci.* **7**, 1719-1724 (2014).
7. A. Serov, Y. S. Kim, M. Odgaard, B. Halevi, P. Atanassov, in *Pacifichem 2015*. (Honolulu, Hi, 2015).
8. M. H. Robson, A. Serov, K. Artyushkova, P. Atanassov, A mechanistic study of 4-aminoantipyrine and iron derived non-platinum group metal catalyst on the oxygen reduction reaction. *Electrochim. Acta* **90**, 656-665 (2013).
9. H. A. Gasteiger, S. S. Kocha, B. Sompalli, F. T. Wagner, Activity benchmarks and requirements for Pt, Pt-alloy, and non-Pt oxygen reduction catalysts for PEMFCs. *Applied Catalysis B: Environmental* **56**, 9-35 (2005).
10. Y. Wang, K. Chen, J. Mishler, S. C. Cho, X. C. Adroher, A review of polymer electrolyte mebrane fuel cells: Technology, applications, and needs on fudamental reseearch. *Applied Energy* **88**, 981-1007 (2011).
11. W. Sheng, H. A. Gasteiger, Y. Shao-Hornb, Hydrogen Oxidation and Evolution Reaction Kinetics on Platinum: Acid vs Alkaline Electrolytes. *Journal of the Electrochemical Society* **157**, B1529-B1536 (2010).
12. N. I. Andersen, A. Serov, P. Atanassov, Metal oxides/CNT nano-composite catalysts for oxygen reduction/oxygen evolution in alkaline media. *Appl. Catal. B-Environ.* **163**, 623-627 (2015).
13. A. Serov, K. Artyushkova, P. Atanassov, Fe-N-C Oxygen Reduction Fuel Cell Catalyst Derived from Carbendazim: Synthesis, Structure, and Reactivity. *Adv. Energy Mater.* **4**, 7 (2014).
14. A. Serov *et al.*, Borohydride-tolerant oxygen electroreduction catalyst for mixed-reactant Swiss-roll direct borohydride fuel cells. *J. Mater. Chem. A* **1**, 14384-14391 (2013).
15. A. Serov, M. H. Robson, M. Smolnik, P. Atanassov, Tri-metallic metal-nitrogen-carbon catlayst derived by sacrificial support method synthesis. *Electrochim. Acta* **109**, 433-439 (2013).
16. U. Tylus *et al.*, Elucidating Oxygen Reduction Active Sites in Pyrolyzed Metal-Nitrogen Coordinated Non-Precious-Metal Electrocatalyst Systems. *J. Phys. Chem. C* **118**, 8999-9008 (2014).

17. U. Tylus *et al.*, Elucidating Oxygen Reduction Active Sites in Pyrolyzed Metal–Nitrogen Coordinated Non-Precious-Metal Electrocatalyst Systems. *The Journal of Physical Chemistry C*, (2014).
18. A. Serov, K. Artyushkova, P. Atanassov, Fe-N-C Oxygen Reduction Fuel Cell Catalyst Derived from Carbendazim: Synthesis, Structure, and Reactivity. *Advanced Energy Materials*, n/a-n/a (2014).
19. U. I. Kramm, M. Lefevre, N. Larouche, D. Schmeisser, J. P. Dodelet, Correlations between Mass Activity and Physicochemical Properties of Fe/N/C Catalysts for the ORR in PEM Fuel Cell via Fe-57 Mossbauer Spectroscopy and Other Techniques. *J. Am. Chem. Soc.* **136**, 978-985 (2014).
20. F. Jaouen *et al.*, Recent advances in non-precious metal catalysis for oxygen-reduction reaction in polymer electrolyte fuel cells. *Energy Environ. Sci.* **4**, 114-130 (2011).
21. S. Kattel, P. Atanassov, B. Kiefer, A density functional theory study of oxygen reduction reaction on non-PGM Fe-Nx-C electrocatalysts. *Phys Chem Chem Phys* **16**, 13800-13806 (2014).
22. S. Kattel, P. Atanassov, B. Kiefer, Density Functional Theory Study of Ni–Nx/C Electrocatalyst for Oxygen Reduction in Alkaline and Acidic Media. *The Journal of Physical Chemistry C* **116**, 17378-17383 (2012).
23. S. Kattel, P. Atanassov, B. Kiefer, Catalytic activity of Co-N(x)/C electrocatalysts for oxygen reduction reaction: a density functional theory study. *Phys Chem Chem Phys* **15**, 148-153 (2013).
24. G. Wu, K. L. More, C. M. Johnston, P. Zelenay, High-performance electrocatalysts for oxygen reduction derived from polyaniline, iron, and cobalt. *Science* **332**, 443-447 (2011).
25. K. Artyushkova, D. Habel-Rodriguez, T. S. Olson, P. Atanassov, Optimization of ink composition based on a non-platinum cathode for single membrane electrode assembly proton exchange membrane fuel cells. *Journal of Power Sources* **226**, 112-121 (2013).
26. A. Serov, M. H. Robson, K. Artyushkova, P. Atanassov, Templated non-PGM cathode catalysts derived from iron and poly(ethyleneimine) precursors. *Applied Catalysis B: Environmental* **127**, 300-306 (2012).
27. N. Ramaswamy, U. Tylus, Q. Jia , S. Mukerjee, Activity Descriptor Identification for Oxygen Reduction on Nonprecious Electrocatalysts: Linking Surface Science to Coordination Chemistry. *J. Am. Chem. Soc.* **135**, (2013).
28. K. Strickland *et al.*, Highly active oxygen reduction non-platinum group metal electrocatalyst without direct metal–nitrogen coordination. *Nature Communications*, (2015).
29. X. Li, G. Liu, B. N. Popov, Activity and stability of non-precious metal catalysts for oxygen reduction in acid and alkaline electrolytes. *Journal of Power Sources* **195**, 6373-6378 (2010).
30. X. Li, B. N. Popova, T. Kawaharab, H. Yanagib, Non-precious metal catalysts synthesized from precursors of carbon, nitrogen, and transition metal for oxygen reduction in alkaline fuel cells. *Journal of Power Sources* **196**, 1717-1722 (2011).

31. M. Alesker *et al.*, Palladium/nickel bifunctional electrocatalyst for hydrogen oxidation reaction in alkaline membrane fuel cell. *Journal of Power Sources* **304**, 332-339 (2016).
32. S. Lu, J. Pan, A. Huang, L. Zhuang, J. Lu, Alkaline polymer electrolyte fuel cells completely free from noble metal catalysts. *PNAS* **105**, 20611-20614 (2008).
33. http://energy.gov/eere/fuelcells/durabilityworgroupking
34. A. Ignaszak, S. Ye, E. Gyenge, A Study of the Catalytic Interface for O2 Electroreduction on Pt: The Interaction between Carbon Support Meso/Microstructure and Ionomer (Nafion) Distribution. *J. Phys. Chem. C* **113**, 298-307 (2009).
35. Y. Liu *et al.*, Proton Conduction and Oxygen Reduction Kinetics in PEM Fuel Cell Cathodes: Effects of Ionomer-to-Carbon Ratio and Relative Humidity Fuel Cells and Energy Conversion. *Journal of Electrochemical Society* **156**, B970-B980 (2009).
36. T. Soboleva, K. Malek, Z. Xie, T. Navessin, S. Holdcroft, PEMFC Catalyst Layers: The Role of Micropores and Mesopores on Water Sorption and Fuel Cell Activity. *ACS Appl. Mater. Interfaces* **3**, 1827-1837 (2011).
37. W. Shi, L. A. Baker, Imaging heterogeneity and transport of degraded Nafion membranes. *Rsc Advances* **5**, 99284-99290 (2015).
38. S. G. Kandlikar, M. L. Garofalo, Z. Lu, Water Management in A PEMFC: Water Transport Mechanism and Material Degradation in Gas Diffusion Layers. *Fuel Cells* **11**, 814-823 (2011).
39. J. Fimrite, Coupled Proton and Water Transport in Polymer Electrolyte Membranes. *Topics in Applied Physics* **113**, 123-198 (2009).
40. C. Y. Ahn, J. Y. Cheon, S. H. Joo, J. Kim, Effects of ionomer content on Pt catalyst/ordered mesoporous carbon support in polymer electrolyte membrane fuel cells. *Journal of Power Sources* **222**, 477-482 (2013).
41. R. N. Bonifacio, A. O. Neto, M. Linardi, Influence of the relative volumes between catalyst and Nafion ionomer in the catalyst layer efficiency. *Int. J. Hydrog. Energy* **39**, 14680-14689 (2014).
42. Q. He, N. S. Suraweera, D. C. Joy, D. J. Keffer, Structure of the Ionomer Film in Catalyst Layers of Proton Exchange Membrane Fuel Cells. *The Journal of Physical Chemistry C* **117**, 25305-25316 (2013).
43. C. Y. Jung, W. J. Kim, S. C. Yi, Optimization of catalyst ink composition for the preparation of a membrane electrode assembly in a proton exchange membrane fuel cell using the decal transfer. *Int. J. Hydrog. Energy* **37**, 18446-18454 (2012).
44. S. Stariha, K. Artyushkova, A. Serov, P. Atanassov, Non-PGM Membrane Electrode Assemblies: Optimization for Performance. *Int. J. Hydrog. Energy* **40**, 14676-14682 (2015).
45. T. S. Olson, K. Chapman, P. Atanassov, Non-platinum cathode catalyst layer composition for single Membrane Electrode Assembly Proton Exchange Membrane Fuel Cell. *Journal of Power Sources* **183**, 557-563 (2008).
46. K. H. Kim *et al.*, The effects of Nafion (R) ionomer content in PEMFC MEAs prepared by a catalyst-coated membrane (CCM) spraying method. *Int. J. Hydrog. Energy* **35**, 2119-2126 (2010).

47. M. A. Hickner, A. M. Herring, E. B. Coughlin, Anion Exchange Membranes: Current Status and Moving Forward. *Journal of Polymer Science, Part B: Polymer Physics* **51**, 1727-1735 (2013).
48. X. Ren, S. C. Price, A. C. Jackson, N. Pomerantz, F. L. Beyer, Highly Conductive Anion Exchange Membrane for High Power Density Fuel-Cell Performance. *Applied Materials & Interfaces* **6**, 13330-13333 (2014).
49. M. Carmo, G. Doubek, R. C. Sekol, M. Linardi, A. D. Taylor, Development and electrochemical studies of membrane electrode assemblies for polymer electrolyte alkaline fuel cells using FAA membrane and ionomer. *Journal of Power Sources* **230**, 169-175 (2013).
50. N. J. Robertson *et al.*, Tunable High Performance Cross-Linked Alkaline Anion Exchange Membranes for Fuel Cell Applications. *J. Am. Chem. Soc.* **132**, 3400-3404 (2010).
51. A. Z. Weber *et al.*, A Critical Review of Modeling Transport Phenomena in Polymer-Electrolyte Fuel Cells. *Journal of the Electrochemical Society* **161**, F1254-F1299 (2014).
52. J. Liu, M. Eikerling, Model of cathode catalyst layers for polymer electrolyte fuel cells: The role of porous structure and water accumulation. *Electrochim. Acta* **53**, 4435-4446 (2008).
53. N. Leonard *et al.*, Modeling of Low-Temperature Fuel Cell Electrodes Using Non-Precious Metal Catalysts. *Journal of Electrochemical Society* **162**, F1253-F1261 (2015).
54. C. Ziegler, S. Thiele, R. Zengerle, Direct three-dimensional reconstruction of a nanoporous catalyst layer for a polymer electrolyte fuel cell. *Journal of Power Sources* **196**, 2094-2097 (2011).
55. Q. Hu *et al.*, Alkaline polymer electrolyte fuel cell with Ni-based anode and Co-based cathode. *Int. J. Hydrog. Energy* **38**, 16264-16268 (2013).
56. M. Carmo, G. Doubek, R. C. Sekol, M. Linardi, A. D. Taylor, Development and electrochemical studies of membrane electrode assemblies for polymer electrolyte alkaline fuel cell using FAA membrane and ionomer. *Journal of Power Sources* **230**, 169-175 (2013).
57. T. Sakamoto *et al.*, Operando XAFS study of carbon supported Ni, NiZn, and Co catalysts for hydrazine electrooxidation for use in anion exchange membrane fuel cells. *Electrochim. Acta* **163**, 116-122 (2015).
58. A. V. Pismenny, Univeristy of Toronto, National Library of Canada (2001).
59. http://www.kratos.com/applications/techniques/x-ray-photoelectron-spectroscopy
60. K. Artyushkova, S. Levendosky, P. Atanassov, J. Fulghum, XPS structural studies of nano-composite non-platinum electrocatalysts for polymer electrolyte fuel cells. *Top. Catal.* **46**, 263-275 (2007).
61. K. Artyushkova, S. Pylypenko, M. Dowlapalli, P. Atanassov, Structure-to-property relationships in fuel cell catalyst supports: Correlation of surface chemistry and morphology with oxidation resistance of carbon blacks. *Journal of Power Sources* **214**, 303-313 (2012).
62. R. Borup, "Durability Improvements Through Degradation Mechism Studies," (DOE 2011 Annual Merit Review Meeting, 2012).

63. A. Serov *et al.*, Nano-structured non-platinum catalysts for automotive fuel cell application. *Nano Energy* **16**, 293-300 (2015).
64. C. Y. Liu, C. C. Sung, A review of the performance and analysis of proton exchange membrane fuel cell membrane electrode assemblies. *Journal of Power Sources* **220**, 348-353 (2012).
65. S. Stariha *et al.*, Non-PGM Fe-N-C Catalysts for Oxygen Reduction Reaction: Catlayst Layer Design. *Journal of Power Sources* **submitted,** (2016).
66. W. J. Whitehouse, The quantitative morphology of anisotropic trabecular bone. *Journal of Microscopy* **101**, 153-168 (1974).
67. H. Beyenal, Z. Lewandowski, G. Harkin, Quantifying biofilm structure: facts and fiction. *Biofouling* **20**, 1-23 (2004).
68. K. Artyushkova *et al.*, Relationship between surface chemistry, biofilm structure, and electron transfer in Shewanella anodes. *Biointerphases* **10**, 019013 (2015).
69. K. Artyushkova, A. Serov, S. Rojas-Carbonell, P. Atanassov, Chemistry of Multitudinous Active Sites for Oxygen Reduction Reaction in Transition Metal-Nitrogen-Carbon Electrocatalysts. *The Journal of Physical Chemistry C*, (2015).
70. A. Zitolo *et al.*, Identification of catalytic sites for oxygen reduction in iron- and nitrogen-doped graphene materials. *Nat Mater* **14**, 937-942 (2015).
71. S. Kabir, K. Artyushkova, A. Serov, B. Kiefer, P. Atanassov, Experimental and Computational Identification of Graphitic-N Moiety Present in Self-Supported Electrocatalysts. *Surf Interface Anal* **submitted**, (2015).
72. J. D. Wiggins-Camacho, K. J. Stevenson, Mechanistic Discussion of the Oxygen Reduction Reaction at Nitrogen-Doped Carbon Nanotubes. *J Phys Chem C* **115**, 20002-20010 (2011).

10. APPENDIX

Catalyst	Conductivity at 1111 psi (S/cm)
Vulcan	344.3
KB600	120.5
CNT	219.1
UR-no carbon	401.6
UR-Vulcan	688.5
UR-KB600	123.6
UR-CNT	102.5
MM-no carbon	253.7
MM-Vulcan	209.5
MM-KB600	126.8
MM-CNT	96.4

Figure A1. Bulk electronic conductivity measurements taken of UR and MM derived catalysts with and without the addition of carbon at 1111 psi.

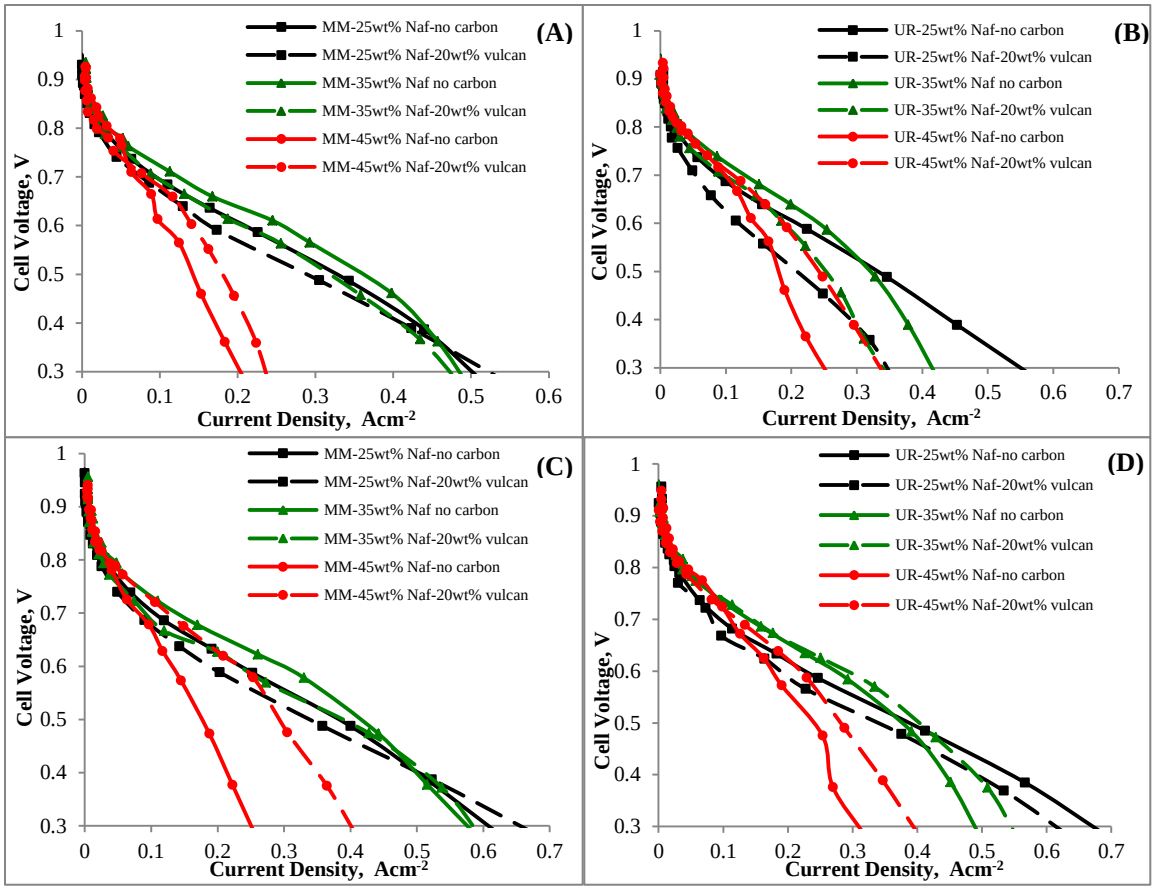

Figure A2. Polarization curves for both catalysts with 25wt%, 35wt%, and 45wt% Nafion® ionomer with 20wt% Vulcan taken in H_2/air **(A)** MM-derived catalyst at 12 $(0.8\ bar)_{gauge}$ psi backpressure**(B)** UR-derived catalyst at 12 $(0.8\ bar)_{gauge}$ psi backpressure **(C)** MM-derived catalyst taken at 30 $(2\ bar)_{gauge}$ psi backpressure **(D)** UR-derived catalyst at 30 $(2\ bar)_{gauge}$ psi backpressure.

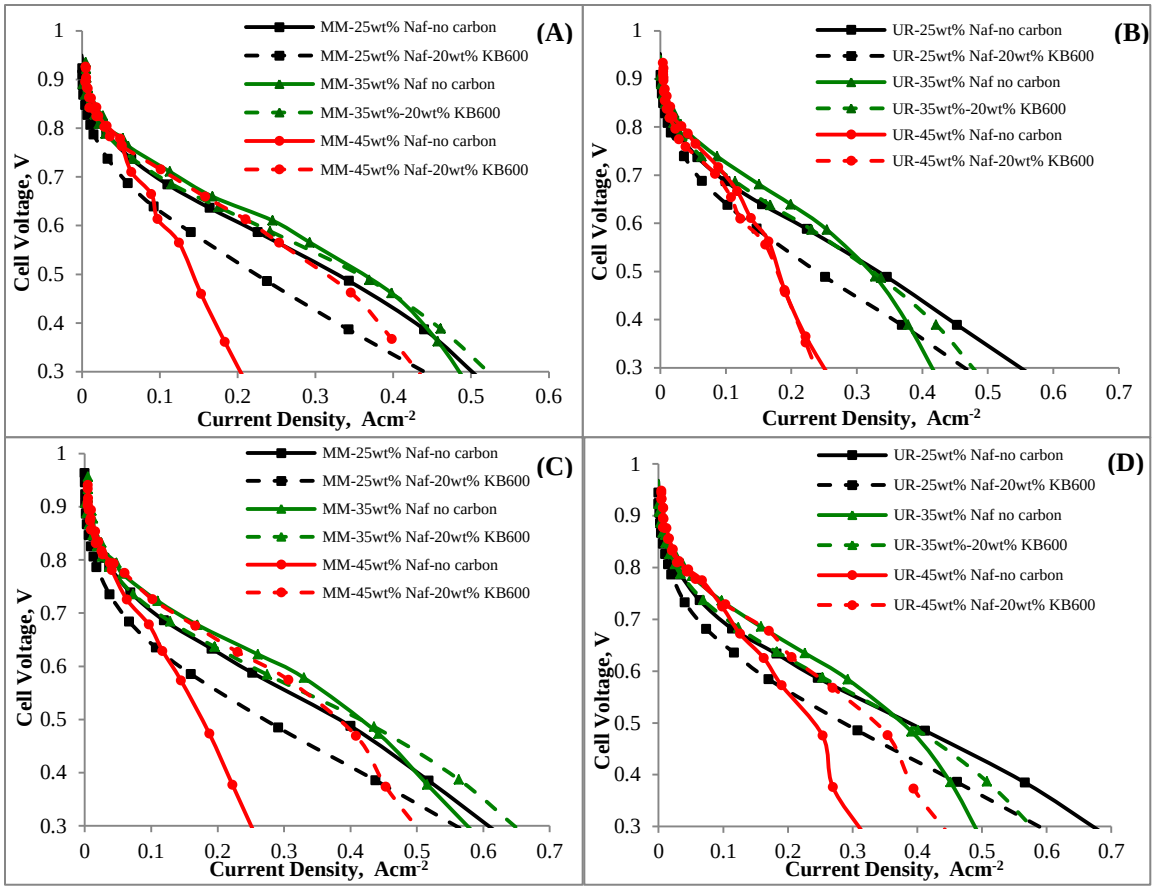

Figure A3. Polarization curves for both catalysts with 25wt%, 35wt%, and 45wt% Nafion® ionomer with 20wt% KB600 taken in H_2/air **(A)** MM-derived catalyst at 12 $(0.8\ \text{bar})_{\text{gauge}}$ psi backpressure **(B)** UR-derived catalyst at 12 $(0.8\ \text{bar})_{\text{gauge}}$ psi backpressure **(C)** MM-derived catalyst taken at 30 $(2\ \text{bar})_{\text{gauge}}$ psi backpressure **(D)** UR-derived catalyst at 30 $(2\ \text{bar})_{\text{gauge}}$ psi backpressure.

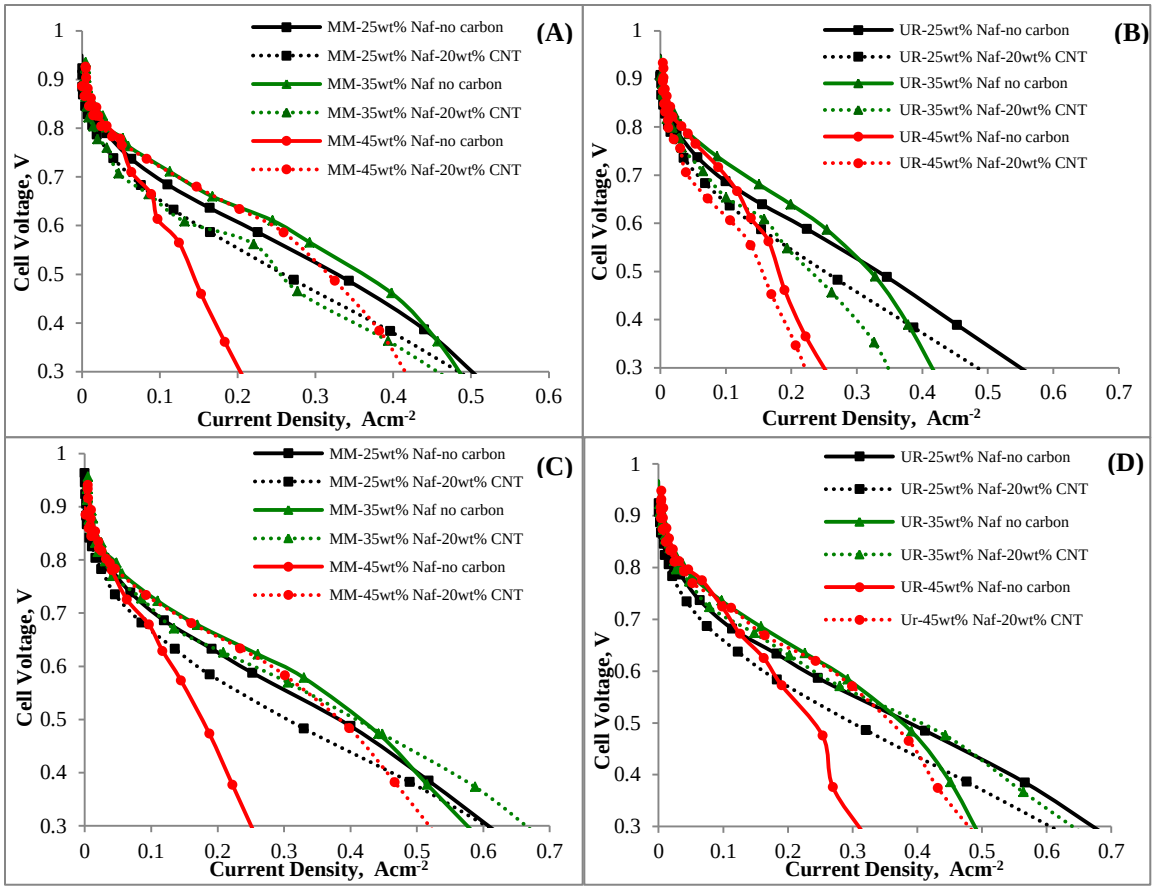

Figure A4. Polarization curves for both catalysts with 25wt%, 35wt%, and 45wt% Nafion® ionomer with 20wt% CNTs taken in H_2/air **(A)** MM-derived catalyst at 12 $(0.8\ bar)_{gauge}$ psi backpressure **(B)** UR-derived catalyst at 12 $(0.8\ bar)_{gauge}$ psi backpressure **(C)** MM-derived catalyst taken at 30 $(2\ bar)_{gauge}$ psi backpressure **(D)** UR-derived catalyst at 30 $(2\ bar)_{gauge}$ psi backpressure.